Inorg. Chem. **2001,** *40,* 687−702

Electronic Spectral Studies of Molybdenyl Complexes. 2. MCD Spectroscopy of $[\mathrm{MoO}\mathit{S}_4]^-$ Centers

Jonathan McMaster,[†,‡] Michael D. Carducci,[†] Yi-Shan Yang,[§] Edward I. Solomon,*,[§] and John H. Enemark*,[†]

Department of Chemistry, University of Arizona, Tucson, Arizona 85721, and Department of Chemistry, Stanford University, Stanford, California 94305

Received May 31, 2000

Magnetic circular dichroism (MCD) and absorption spectroscopies have been used to probe the electronic structure of $[\mathrm{PPh}_4][\mathrm{MoO}(p\text{-}\mathrm{SC}_6\mathrm{H}_4\mathrm{X})_4]$ (X = H, Cl, OMe) and $[\mathrm{PPh}_4][\mathrm{MoO(edt)}_2]$ complexes (edt = ethane-1,2-dithiolate). The results of density functional calculations (DFT) on $[\mathrm{MoO(SMe)}_4]^-$ and $[\mathrm{MoO(edt)}_2]^-$ model complexes were used to provide a framework for the interpretation of the spectra. Our analysis shows that the lowest energy transitions in $[\mathrm{Mo^VO}\mathit{S}_4]$ chromophores (S_4 = sulfur donor ligand) result from S → Mo charge transfer transitions from S valence orbitals that lie close to the ligand field manifold. The energies of these transitions are strongly dependent on the orientation of the S lone-pair orbitals with respect to the Mo atom that is determined by the geometry of the ligand backbone. Thus, the lowest energy transition in the MCD spectrum of $[\mathrm{PPh}_4][\mathrm{MoO}(p\text{-}\mathrm{SC}_6\mathrm{H}_4\mathrm{X})_4]$ (X = H) occurs at 14 800 cm^{-1}, while that in $[\mathrm{PPh}_4][\mathrm{MoO(edt)}_2]$ occurs at 11 900 cm^{-1}. The identification of three bands in the absorption spectrum of $[\mathrm{PPh}_4][\mathrm{MoO(edt)}_2]$ arising from LMCT from S pseudo-σ combinations to the singly occupied Mo 4d orbital in the *xy* plane suggests that there is considerable covalency in the ground-state electronic structures of $[\mathrm{MoO}\mathit{S}_4]$ complexes. DFT calculations on $[\mathrm{MoO(SMe)}_4]^-$ reveal that the singly occupied HOMO is 53% Mo $4d_{xy}$ and 35% S p for the equilibrium C_4 geometry. For $[\mathrm{MoO(edt)}_2]^-$ the steric constraints imposed by the edt ligands result in the S π orbitals being of similar energy to the Mo 4d manifold. Significant S pseudo-σ and π donation may also weaken the Mo≡O bond in $[\mathrm{MoO}\mathit{S}_4]$ centers, a requirement for facile active site regeneration in the catalytic cycle of the DMSO reductases. The strong dependence of the energies of the bands in the absorption and MCD spectra of $[\mathrm{PPh}_4][\mathrm{MoO}(p\text{-}\mathrm{SC}_6\mathrm{H}_4\mathrm{X})_4]$ (X = H, Cl, OMe) and $[\mathrm{PPh}_4][\mathrm{MoO(edt)}_2]$ on the ligand geometry suggests that the structural features of the active sites of the DMSO reductases may result in an electronic structure that is optimized for facile oxygen atom transfer.

I. Introduction

Mo is associated with more than 30 enzymes that catalyze key two-electron oxidation−reduction reactions in the metabolism of C, N, and S by microorganisms, plants, and animals.[1,2] Protein X-ray crystal structures[3−13] and EXAFS[14−18] and EPR[19−22] spectroscopies confirm that there are three distinct structural families for the Mo centers.[2] The active sites of the sulfite oxidase and xanthine oxidase families contain *one* novel pyranopterin dithiolate unit (Figure 1)[23,24] per Mo, whereas

---

[†] University of Arizona.

[‡] Current address: School of Chemistry, University of Nottingham, Nottingham, NG7 2RD, United Kingdom.

[§] Stanford University.

(1) Pilato, R. S.; Stiefel, E. I. In *Bioinorganic Catalysis*; Reedijk, J., Ed.; Marcel Dekker Inc.: New York, 1993.

(2) Hille, R. *Chem. Rev.* **1996**, *96*, 2757−2816.

(3) Romão, M. J.; Archer, M.; Moura, I.; Moura, J. J. G.; LeGall, J.; Engh, R.; Schneider, M.; Hof, P.; Huber, R. *Science* **1995**, *270*, 1170−1176.

(4) Huber, R.; Hof, P.; Duarter, R. O.; Moura, J. J. G.; Moura, I.; Liu, M. Y.; Legall, J.; Hille, R.; Archer, M.; Romão, M. *Proc. Natl. Acad. Sci. U.S.A* 1996, *93*, 8846−8851.

(5) Kisker, C.; Schindelin, H.; Rees, D. C. *Annu. Rev. Biochem.* **1997**, *66*, 233−267.

(6) Schneider, F.; Lowe, J.; Huber, R.; H. S.; Kisker, C.; Knablien, J. *J. Mol. Biol.* **1996**, *263*, 53−59.

(7) McAlpine, A. S.; McEwan, A. G.; Shaw, A. L.; Bailey, S. *J. Biol. Inorg. Chem.* **1997**, *2*, 690−701.

(8) Kisker, C.; Schindelin, H.; Pacheco, A.; Wehbi, W. A.; Garrett, R. M.; Rajagopalan, K. V.; Enemark, J. H.; Rees, D. C. *Cell* **1997**, *91*, 973−983.

(9) Boyington, J. C.; Gladyshev, V. N.; Khangulov, S. V.; Stadtman, T. C.; Sun, P. D. *Science* **1997**, *275*, 1305−1308.

(10) McAlpine, A. S.; McEwan, A. G.; Bailey, S. *J. Mol. Biol.* **1998**, *275*, 613−623.

(11) Czjzek, M.; Dos Santos, J.-P.; Pommier, J.; Giordano, G.; Méjean, V.; Haser, R. *J. Mol. Biol.* **1998**, *284*, 435−447.

(12) Dias, J. M.; Than, M. E.; Humm, A.; Huber, R.; Bourenkov, G. P.; Bartunik, H. D.; Bursakov, S.; Calvete, J.; Caldeira, J.; Carneiro, C.; Moura, J. J. G.; Moura, I.; Romão, M. J. *Structure* **1999**, *7*, 65−79.

(13) Dobbek, H.; Gremer, L.; Meyer, O.; Huber, R. *Proc. Natl. Acad. Sci. U.S.A.* **1999**, *96*, 8884−8889.

(14) George, G. N.; Kipke, C. A.; Prince, R. C.; Suede, R. A.; Enemark, J. H.; Cramer, S. P. *Biochemistry* **1989**, *28*, 5075−5080.

(15) Cramer, S. P.; Wahl, R.; Rajagopalan, K. V. *J. Am. Chem. Soc.* **1981**, *103*, 7721−7727.

(16) George, N. G.; Hilton, J.; Rajagopalan, K. V. *J. Am. Chem. Soc* **1996**, *118*, 1113−1117.

(17) Baugh, P. E.; Garner, C. D.; Charnock, J. M.; Collison, D.; Davies, E. S.; McAlpine, A. S.; Bailey, S.; Lane, I.; Hanson, G. R.; McEwan, G. *J. Biol. Inorg. Chem.* **1997**, *2*, 634−643.

(18) George, G. N.; Hilton, J.; Temple, C.; Prince, R. C.; Rajagopalan, K. V. *J. Am. Chem. Soc.* **1999**, *121*, 1256−1266.

(19) Bennett, B.; Benson, N.; McEwan, A. G.; Bray, R. C. *Eur. J. Biochem.* **1994**, *225*, 321−331.

(20) Bray, R. C.; Bennett, B.; Burke, J. F.; Chovnick, A.; Doyle, W. A. *Biochem. Soc. Trans.* **1997**, *24*, 999−105.

(21) Howes, B. D.; Bray, R. C.; Richards, R. L.; Turner, N. A.; Bennett, B.; Lowe, D. J. *Biochemistry* **1996**, *35*, 1432−1443.

(22) Dhawan, I. K.; Pacheco, A.; Enemark, J. H. *J. Am. Chem. Soc.* **1994**, *116*, 7911−7912.

(23) Rajagopalan, K. V. *Adv. Enzymol. Relat. Areas Mol. Biol.* **1991**, *64*, 215−289.

(24) Fischer, B.; Enemark, J.; Basu, P. *J. Inorg. Biochem.* **1998**, *72*, 13-21.

10.1021/ic0005846 CCC: \$20.00

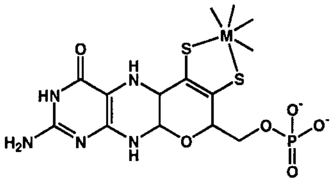

Figure 1. The structure of the pyranopterin dithiolate (molybdopterin) unit showing its coordination mode to M = Mo or W. In enzymes from prokaryotic sources cytosine, adenine, or guanine dinucleotides may be attached via a pyrophosphate linkage.

members of the DMSO reductase family[6,7,9−12] have *two* pyranopterin dithiolate units per Mo atom. The coordination of the Mo centers of the oxidized forms of DMSO reductase from *Rhodobacter capsulatus* (*Rc*)[6,7,10] and *Rhodobacter sphaeroides* (*Rs*)[25] is completed by at least one terminal oxo ligand and a coordinated serine residue.

One of the proposed catalytic mechanisms for DMSO reductase involves a cycling of the active site between the mono-oxo-Mo(VI) and *des*-oxo-Mo(IV) forms through a *des*-oxo-Mo(V) state.[18,26] Support for this mechanism derives from resonance Raman spectroscopic[26] and EXAFS[18] studies on DMSO reductase from *Rs* that also suggest that the bis(ene-1,2-dithiolate) ligation to Mo from the pyranopterinin dithiolate unit (Figure 1) is maintained in the diamagnetic Mo(IV) and Mo(VI) states and paramagnetic Mo(V) states in all the phases of the catalytic cycle.

Low temperature MCD spectroscopy is an extremely powerful technique for investigating the electronic structure of the *ground and excited states* of paramagnetic metal centers.[27−29] MCD spectroscopy complements traditional absorption and EPR spectroscopies by probing the effects of Zeeman splitting on the ground and the excited states of the metal center. This additional information can provide definitive assignments of spectroscopic transitions and help to deconvolute overlapping components. Preliminary variable temperature (VT) MCD spectra for desulfo inhibited xanthine oxidase provided encouraging evidence that MCD spectroscopy could be used to study the Mo centers of enzymes, despite the presence of other more strongly absorbing chromophores.[30] Recently, difference MCD methods have been used to study the “very rapid” intermediate in xanthine oxidase[31] and to probe the Mo(V) state of sulfite oxidase in the presence of its *b*-type heme center.[32] The DMSO reductases from *Rc*[33] and *Rs*[34] contain the Mo cofactor as the only prosthetic group, and low-temperature MCD studies of their ethylene glycol inhibited Mo(V) states have revealed rich and distinctive spectroscopic features between 12 500 and 34 000 cm^{-1}.[33,34] These spectra were originally interpreted using a fragment of C_{2v} symmetry in which a *single* ene-1,2-dithiolate is coordinated to Mo(V). The spectra have not been reinterpreted in the view of the recent X-ray crystallographic results that show two ene-1,2-dithiolate ligands per Mo atom. VTMCD studies have also been carried out on the tungsten-containing aldehyde ferredoxin oxidoreductase from *Pyrococcus furiosus*,[35] revealing an MCD spectrum for the ethylene glycolate inhibited form similar to those of the DMSO reductases. However, the interpretation of the VTMCD spectra for the native enzyme was complicated by inhomogeneities at the active site.

An understanding of the electronic structures of well-characterized molybdenyl ($[\mathrm{MoO}]^{3+}$) complexes is an essential prerequisite to interpreting the spectroscopy and function of the Mo active sites in enzymes. A self-consistent picture of the electronic structure of $[\mathrm{MoOX}_4]^-$ (X = F, Cl, Br)[36−38] and the analogous V, Cr, and W compounds has emerged from solution and single-crystal EPR,[36,39] UV/vis absorption,[38,40,41] and MCD spectroscopic studies on these systems.[41,42] These studies have been supported by theoretical calculations,[43−47] utilizing principally density functional approaches,[45,47,48] that have proved to be critical in providing a framework for the interpretation of the spectroscopic results. The conclusions support dominant oxo-Mo bonding in the electronic structure of the $[\mathrm{MoOX}_4]^-$ chromophore, resulting in a $d_{xy} < d_{xz,yz} < d_{x^2-y^2} < d_{z^2}$ energy order for the d orbital manifold with the unpaired electron residing in the Mo 4d_{xy} orbital. Intense LMCT to the Mo 4d_{xy} orbital occurs from the essentially nonbonding lone pair orbitals that are localized on the equatorial atoms and that lie below the ligand field manifold.[41,42] The excited states associated with these transitions have been recognized as being important contributors to the g values of $[\mathrm{MoOX}_4]^-$ complexes.[47]

A recognition of S ligation to Mo at the active sites of Mo-containing enzymes prompted investigations into the electronic structures of $(\mathrm{L-N_3})\mathrm{MoO}S_2$ complexes [$\mathrm{L-N_3}$ = hydrotris(3,5-dimethyl-1-pyrazolyl)borate, S_2 = mono or bidentate S ligand].[49,50,51] EPR spectroscopy on these compounds reveals geometry dependent g_z values that often exceed $g_e = 2.0023$,[50−52] which suggests that there is considerable S character in the Mo 4d_{xy} orbital in $(\mathrm{L-N_3})\mathrm{MoO}S_2$ complexes. PES studies on $(\mathrm{L-N_3})\mathrm{MoO}S_2$ compounds also support a S-rich ground state, and comparative studies of $(\mathrm{L-N_3})\mathrm{ME}S_2$ (E = O, S, NO) com-

---

(25) Schindelin, H.; Kisker, C.; Hilton, J.; Rajagopalan, K.; Rees, D. C. *Science* 1996, *272*, 1615−1621.

(26) Garton, S. D.; Hilton, J.; Oku, H.; Crouse, B. R.; Rajagopalan, K. V.; Johnson, M. K. *J. Am. Chem. Soc.* **1997**, *119*, 12906−12916.

(27) Stephens, P. J. *Annu. Rev. Phys. Chem.* **1974**, *25*, 201−232.

(28) Sutherland, J. C.; Holmquist, B. *Annu. Rev. Biophs. Bioeng.* **1980**, *9*, 293−326.

(29) Piepho, S. B.; Schatz, P. N. *Group Theory in Spectroscopy with Applications to Magnetic Circular Dichroism*; Wiley-Interscience: New York, 1983.

(30) Peterson, J.; Godfrey, C.; Thomson, A. J.; George, G. N.; Bray, R. C. *Biochem. J.* **1986**, *233*, 107−110.

(31) Jones, R. M.; Inscore, F. E.; Hille, R.; Kirk, M. L. *Inorg. Chem.* **1999**, *38*, 4963−4970.

(32) Helton, M. E.; Pacheco, A.; McMaster, J.; Enemark, J. H.; Kirk, M. L. *J. Inorg. Biochem.* **1999**, *80*, 227−233.

(33) Benson, N.; Farrar, J. A.; McEwan, A. G.; Thomson, A. J. *FEBS Lett.* **1992**, *307*, 169−172.

(34) Finnegan, M. G.; Hilton, J.; Rajagopalan, K. V.; Johnson, M. K. *Inorg. Chem.* **1993**, *32*, 2616−2617.

(35) Koehler, B. P.; Mukund, S.; Conover, R. C.; Dhawan, I. K.; Roy, R.; Adams, M. W. W.; Johnson, M. K. *J. Am. Chem. Soc.* **1996**, *118*, 12391−12405.

(36) Garner, C. D.; Hill, L. H.; Mabbs, F. E.; McFadden, D. L.; McPhail, A. T. *J. Chem. Soc., Dalton Trans.* **1977**, 1202−1207.

(37) Gray, H. B.; Hare, C. R. *Inorg. Chem.* **1962**, *1*, 363−368.

(38) Collison, D. *J. Chem. Soc., Dalton Trans.* **1990**, 2999−3006.

(39) Garner, C. D.; Hillier, I. H.; Mabbs, F. E.; Taylor, C.; Guest, M. F. *J. Chem. Soc., Dalton Trans.* **1976**, 2258−2261.

(40) Collison, D.; Gahan, B.; Garner, C. D.; Mabbs, F. E. *J. Chem. Soc., Dalton Trans.* **1980**, 667−674.

(41) Carducci, M. D.; Brown, C.; Solomon, E. I.; Enemark, J. H. *J. Am. Chem. Soc.* **1994**, *116*, 11856−11868.

(42) Sabel, D. M.; Gewirth, A. A. *Inorg. Chem.* **1994**, *33*, 148−156.

(43) Sunil, K. K.; Harrison, J. F.; Rogers, M. T. *J. Chem. Phys.* **1982**, *76*, 3087−3097.

(44) Weber, J.; Garner, C. D. *Inorg. Chem.* **1980**, *19*, 2206−2209.

(45) Deeth, R. J. *J. Chem. Soc., Dalton Trans.* **1991**, 1895−1900.

(46) Balagopalakrishna, C.; Kimbrough, J. T.; Westmoreland, T. D. *Inorg. Chem.* **1996**, *35*, 7758−7768.

(47) Swann, J.; Westmoreland, T. D. *Inorg. Chem.* **1997**, *36*, 5348−5357.

(48) Ziegler, T. *Chem. Rev.* **1991**, *91*, 651−667.

(49) Enemark, J. H.; Young, C. G. *Adv. Inorg. Chem.* **1993**, *40*, 1−88.

(50) Cleland, W. E., Jr.; Barnhart, K. M.; Yamanouchi, K.; Collison, D.; Mabbs, F. E.; Ortega, R. B.; Enemark, J. H. *Inorg. Chem.* **1987**, *26*, 1017−1025.

(51) Chang, C. S. J.; Collison, D.; Mabbs, F. E.; Enemark, J. H. *Inorg. Chem.* **1990**, *29*, 2261−2267.

(52) Dhawan, I. K.; Enemark, J. H. *Inorg. Chem.* **1996**, *35*, 4873−4882.

plexes suggest an "electronic buffer" role for the ene-1,2-dithiolate ligand during formal metal oxidation state changes that may occur during enzyme turnover.[53] Optical and MCD spectroscopies on $(L-N_3)MoOS_2$ complexes[41] expose the presence of low energy S → Mo LMCT bands at 9000−12 000 cm^{-1}, and parallel MCD and resonance Raman studies on $(L-N_3)MoO(bdt)$[54] (bdt = benzene-1,2-dithiolate) identify a covalent three-center pseudo-σ interaction between the redox active Mo $4d_{xy}$ orbital and an S in-plane symmetry adapted linear combination (SALC). This interaction may provide a mechanism for coupling the Mo redox active orbital with the in-plane orbitals of the pyranopterin at the active sites of oxomolybdenum enzymes that allows for a modulation of the reduction potential at the Mo center and for a σ-type electron-transfer pathway for active site regeneration.[54]

The presence of a $[Mo(ene\text{-}1,2\text{-}dithiolate)_2]$ unit at the active site of the formally Mo(VI) and Mo(IV) forms of the DMSO reductases from *Rc*[6,7,10] and *Rs*[25] (and other members of this family of molybdoenzymes[9,11,12]) points to the need for fundamental investigations of the electronic structures of Mo(V) centers with *four* S donors in order to evaluate the LMCT transitions in $[MoOS_4]$ centers (S = sulfur donor ligand) as a probe of electronic structure. In particular, MCD spectroscopy of structurally well-characterized $[Mo^VOS_4]$ compounds should provide a starting point for future reevaluation of the MCD spectra of the Mo(V) centers of the DMSO reductases.

Extensive EPR, UV/vis absorption, and X-ray crystallographic data are available for $[MoO(SPh)_4]^-$ and $[MoO(edt)_2]^-$ (edt = ethane-1,2-dithiolate). The X-ray crystal structures of $[AsPh_4][MoO(SPh)_4]$[55] and $[PPh_4][MoO(edt)_2]$[56] reveal a $[MoO]^{3+}$ unit coordinated by four S donors in a square pyramidal geometry of approximately C_4 and C_{2v} symmetry for $[MoO(SPh)_4]^-$ and $[MoO(edt)_2]^-$, respectively. The g_z values for $[MoO(SPh)_4]^-$ (2.017) and $[MoO(edt)_2]^-$ (2.052), determined by EPR spectroscopy,[52,57,58] exceed g_e, and their visible spectra reveal intense LMCT bands around 16 000 cm^{-1}.[56,57,59] MCD spectra for $[MoO(SPh)_4]^-$ and $[MoO(edt)_2]^-$ were first recorded in 1986;[60] more recently, MCD spectra for $[MoO(bdt)_2]^-$ [61,62] and $[WO(bdt)_2]^-$ were reported.[61]

Given the prevalence of $[MoOS_4]$ coordination in the oxidized and reduced forms of the DMSO reductases and to extend the previous work on $(L-N_3)MoOS_2$ systems, we report the MCD investigations of $[PPh_4][MoO(p\text{-}SC_6H_4X)_4]$ (X = H, Cl, OMe) and $[PPh_4][MoO(edt)_2]$. These studies, which build upon the previous work on $(L-N_3)MoOS_2$ systems,[41,50−54] use density functional electronic models to aid in the interpretation of the MCD spectra and to obtain insight concerning the electronic structures of $[MoOS_4]$ cores. While this paper was in review, assignments of the MCD spectra of three complexes with $[Mo^VOS_4]$ cores were independently reported by Kirk and coworkers.[63,64]

II. Experimental Section

1. Preparation of Compounds. All reactions were carried out under an Ar atmosphere using standard Schlenk line techniques. Tetrahydrofuran was dried and distilled from sodium and benzophenone, methanol from magnesium turnings, dichloromethane from calcium hydride, 1,2-dichloroethane from calcium hydride, and diethyl ether from sodium and benzophenone. $[PPh_4][MoO(SPh)_4]$,[65] $[PPh_4][MoO(p\text{-}SC_6H_4Cl)_4]$,[66] and $[PPh_4][MoO(edt)_2]$[56] were prepared according to literature methods. $[PPh_4][MoO(p\text{-}SC_6H_4OMe)_4]$ was prepared using the same procedure as for $[PPh_4][MoO(SPh)_4]$[65] but with the substitution of $p\text{-}MeOC_6H_4SH$ for PhSH. We found this compound to be relatively unstable, decomposing within 4 h in degassed dichloromethane under Ar. A degassed 1:1 mixture of 1,2-dichloroethane/DMF was used as the glassing solution for all the complexes for both the frozen solution EPR and MCD experiments. A degassed dichloromethane solution was used for the room-temperature absorption measurements.

2. Absorption, MCD, and EPR Studies. Room-temperature absorption spectra of the complexes were obtained on an OLIS 4300S modified Cary 14 UV/vis/near-IR spectrophotometer. MCD spectra in the 2500−8500 Å region were collected on a JASCO J-500C CD spectropolarimeter configured with focusing optics and an Oxford cryostat/SM4−7T magnet capable of producing fields up to 7.0 T and sample temperatures down to 1.5 K. For the 6000−20 000 Å region, MCD spectra were collected on a JASCO J-200C CD spectropolarimeter configured with focusing optics and an Oxford cryostat/SM4000-7T magnet capable of producing fields up to 7.0 T and sample temperatures down to 1.5 K. Glasses were prepared by injecting ~0.25 mL of the solution of the compound dissolved in the glassing solvent into a cell comprised of two quartz disks sandwiching a rubber O-ring of thickness 2 mm. Depolarization of the beam was checked for each sample by measuring the CD spectrum of a standard nickel (+)-tartrate solution with the sample positioned in the beam both before and after the standard.[29] Samples which decreased the CD signal by less than 10% were considered suitable. Unless otherwise stated, all MCD spectra were obtained at magnetic fields of 5 T and at a stable (±0.2 K) temperature between 4.2 and 6 K.

X-band EPR spectra were recorded on a Bruker ESP 300 spectrometer as frozen glass solutions. The spectra were simulated using the program QPOW.[67] Anisotropic g values and approximate line widths for the $I = 0$ components were simulated to give the best visual fit. The anisotropic $A(^{95,97}Mo)$ hyperfine splittings were then simulated separately ($I = 5/2$ component only) at anisotropic g values fixed at the values previously determined for the $I = 0$ component. The $A(^{95,97}Mo)$ components and the line widths were varied to obtain a reasonable fit. The $I = 0$ and $I = 5/2$ simulated spectra were then integrated separately and contributions from the $I = 0$ ($^{92,94,96,98}Mo$, 75% abundant) and the $I = 5/2$ ($^{95,97}Mo$, 25% abundant) components were summed in the ratio 3:1. The derivative of this composite simulated spectrum was compared to the experimental spectrum. It was assumed that the $\mathbf{g}$ and $\mathbf{A}(^{95,97}\mathbf{Mo})$ tensors were coincident (the Euler angles α, β, and $\gamma = 0$) due to the reasonably high symmetry of $[MoO(SPh)_4]^-$ and $[MoO(edt)_2]^-$.

3. Computational Details. The $[MoO(SPh)_4]^-$ anion possesses approximately C_4 symmetry in the crystal structure of $[AsPh_4][MoO(SPh)_4]$.[55] The average O−Mo−S−C(α) dihedral angle of 58.8° gives rise to a propeller configuration for the ligands about the Mo=O unit,

---

(53) Westcott, B. L.; Gruhn, N. E.; Enemark, J. H. *J. Am. Chem. Soc.* **1998**, *120*, 3382−3386.

(54) Inscore, F. E.; McNaughton, R.; Westcott, B. L.; Helton, M. E.; Jones, R.; Dhawan, I. K.; Enemark, J. H.; Kirk, M. L. *Inorg. Chem.* **1999**, *38*, 1401−1410.

(55) Bradbury, J. R.; Mackay, M. F.; Wedd, A. G. *Aust. J. Chem.* **1978**, *31*, 2423−2430.

(56) Ellis, S. R.; Collison, D.; Garner, C. D.; Clegg, W. *J. Chem. Soc., Chem. Commun.* **1986**, 1483−1485.

(57) Hanson, G. R.; Brunette, A. A.; McDonell, A. C.; Murray, K. S.; Wedd, A. G. *J. Am. Chem. Soc.* **1981**, *103*, 1953−1959.

(58) Hanson, G. R.; Wilson, G. L.; Bailey, T. D.; Pilbrow, J. R. *J. Am. Chem. Soc.* **1987**, *109*, 2609−2616.

(59) Boyde, S.; Ellis, S. R.; Garner, C. D.; Clegg, W. *J. Chem. Soc., Chem. Commun.* **1986**, 1541−1543.

(60) Goodwin A., Ph.D. Thesis, University of Manchester, Manchester, UK, 1986.

(61) Johnson, M. K.; Rees, D. C.; Adams, M. W. W. *Chem. Rev.* **1996**, *96*, 2817−2840.

(62) McNaughton, R. L.; Rubie, N. D.; Helton, M. E.; Kirk, M. L. *J. Inorg. Biochem.* **1999**, *74*, 230.

(63) McNaughton, R. L.; Tipton, A. A.; Rubie, N. D.; Conry, R. R.; Kirk, M. L. *Inorg. Chem.* **2000**, *39*, 5697−5706.

(64) McNaughton, R. L.; Helton, M. E.; Rubie, N. D.; Kirk, M. L. *Inorg. Chem.* **2000**, *39*, 4386-4387.

(65) Boyd, I. W.; Dance, I. G.; Murray, K. S.; Wedd, A. G. *Aust. J. Chem.* **1978**, *31*, 279−284.

(66) Ellis, S. R.; Collison, D.; Garner, C. D. *J. Chem. Soc., Dalton Trans.* **1989**, 413−417.

(67) Nigles, M. J., Ph. D Thesis, University of Illinois, 1979.

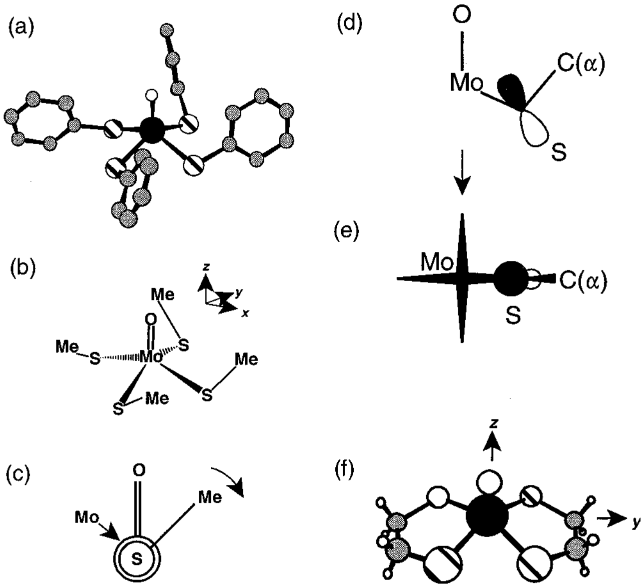

Figure 2. (a) The structure of the $[MoO(SPh)_4]^-$ anion.[55] (b) The model geometry and coordinate frame for $[MoO(SMe)_4]^-$ used in the DFT calculations. Metrical parameters were derived from the X-ray crystallographic coordinates of $[MoO(SPh)_4]^-$ [55] and idealized to C_4 symmetry. (c) Projection along the S−Mo bond for one of the MeS ligands of the model system showing the sense of the synchronous rotations of the four MeS ligands and the pertinent O−Mo−S−C(α) dihedral angle used to derive the Walsh diagram (Figure 6). At a dihedral angle of 0° the S-Me bond is parallel to the Mo═O bond. (d) A S pseudo-σ interaction viewed normal to the Mo═O bond. (e) The orientation of a S pseudo-σ orbital as viewed along the Mo═O bond for O−Mo−S−C(α) = 0°. (f) The model geometry and coordinate frame for $[MoO(edt)_2]^-$ used in the DFT calculations. Metrical parameters were derived from the X-ray crystallographic coordinates of $[MoO(edt)_2]^-$ [56] and idealized to C_{2v} symmetry.

Figure 2a. A $[MoO(SMe)_4]^-$ model (Figure 2b) was adopted for the DFT calculations using a geometry derived from the $[PPh_4][MoO(SPh)_4]$ crystal structure idealized to C_4 symmetry. However, MO calculations were performed under C_2 because of ADF software symmetry restrictions,[68,69] using the coordinate frame defined in Figure 2b. An assessment of the impact of the O−Mo−S−C(α) dihedral angle on the energies within the frontier orbital manifold was made by varying this angle between 0° (C_{4v} symmetry) and 90° (C_4 symmetry) for all four ligands in a clockwise manner as viewed down the S−Mo axes (Figure 2b,c). All values of the dihedral angle involve pseudo-σ interactions with S lone-pair orbitals, as illustrated in Figure 2d,e for O−Mo−S−C(α) = 0°. DFT calculations on $[MoO(edt)_2]^-$ employed atomic coordinates derived from the crystal structure of $[PPh_4][MoO(edt)_2]$[56] idealized to C_{2v} symmetry (Figure 2f). The axis system was chosen so that the z-axis was collinear with the Mo═O bond and the y-axis bisected the S−Mo−S bond angle formed by one edt^{2-} chelate (Figure 2f). The molecular coordinates of $[MoO(SPh)_4]^-$ and $[MoO(edt)_2]^-$ are given in Tables S1 and S2.

Restricted and unrestricted single point calculations were performed using the Amsterdam Density Functional (ADF) suite version 2.3.0[68,69] on an IBM R/S 6000-590 computer. The density functional calculations employed Slater type orbital (STO) triple-ζ-plus polarization basis sets (from the Basis(IV) database of the ADF suite), the frozen core approximation (up to and including 3d for Mo, 2p for S, and 1s for C and O), and the local density approximation (LDA) with the correlation potential due to Vosko et al.[70] Gradient corrections were performed using the functionals of Becke[71] and Perdew.[72] Estimates of transition energies were made using the Slater transition state formalism in which the energy of an electronic transition is determined by the orbital-energy difference from a calculation where the population of the ground-state orbital is decreased by 0.5 and that of the excited state increased by 0.5.[73]

Table 1. Solution Absorption and Frozen Glass MCD Spectral Data for $[PPh_4][MoO(SPh)_4]$

band[a]	energy/cm^{-1} MCD[b]	UV/vis[c]	f_{exptl}	assignments[a,b]
1	14 800 (+)	16 300	0.08	$b(\pi)\rightarrow b(d_{xy})$ (+) $e(\pi)\rightarrow b(d_{xy})$ (+)
2	16 300 (−)			$e(\pi)\rightarrow b(d_{xy})$ (±) $b(d_{xy})\rightarrow e(d_{xz,yz})$ (−)
3	18 100 (+)			$b(d_{xy})\rightarrow e(d_{xz,yz})$ (+)
4	21 000 (+)	22 350	0.02	e(pseudo-σ)$\rightarrow b(d_{xy})$ (+)
5	22 900 (−)			(−)
6	26 500 (−)	intense absorptions	–	a(pseudo-σ)$\rightarrow b(d_{xy})$ (−)
7	28 300 (+)			b(pseudo-σ)$\rightarrow b(d_{xy})$ (+)
8	29 800 (−)			$e(\pi)\rightarrow e(d_{xz,yz})$ (−)
9	31 500 (+)			(+)
10	33 300 (−)			$a,b(\pi)\rightarrow e(d_{xz,yz})$ (−)
11	36 000 (+)			(+)

[a] The band numbers refer to features in the MCD spectrum of $[PPh_4][MoO(SPh)_4]$ (Figure 3). [b] 1,2-dichloroethane/DMF (1:1) frozen glass solution, 5 T, 4.2 K; the signs of the MCD transitions are given in parentheses. [c] CH_2Cl_2 solution, 298 K;

Ab initio HF calculations on geometry-optimized structures for p-$SC_6H_4X^-$ were performed to assess the relative energies of the S lone-pair orbitals for X = H, Cl, OMe. The calculations used the Gaussian94[74] suite of programs and employed a 6-31G** basis set.

III. Results and Analysis

1. Absorption, MCD, and EPR Spectroscopy. A. $[PPh_4][MoO(p\text{-}SC_6H_4X)_4]$ (X = H, Cl, OMe). The room-temperature CH_2Cl_2 solution absorption spectra and 1,2-dichloroethane/DMF (1:1) frozen glass MCD spectra at 4.2 K and 5 T of $[PPh_4][MoO(p\text{-}SC_6H_4X)_4]$ (X = H, Cl, OMe) from 37 000 to 11 700 cm^{-1} are shown in Figure 3a,b. The energies of the MCD and absorption bands for X = H are presented in Table 1. The numbering of the bands in this table refers to features in the MCD spectrum (Figure 3b) and the energies and experimental oscillator strengths, f_{exptl}, of the absorption bands, also shown in Table 1, derive from Gaussian devolved spectra (see below, Figure 11). There are no observable peaks in the absorption or MCD spectra from 12 500 to 7100 cm^{-1} (not shown). The bands within the MCD spectrum all show a $1/T$ (T = temperature) dependence in the linear region of the magnetization-saturation curve that may be fitted with an isotropic $g \approx 2.0$, which is indicative of a Mo(V) ground state.[29] For X = H, a strong postive−negative−positive pattern (bands 1, 2, and 3) dominates the MCD spectrum from 15 000 to 20 000 cm^{-1} (Figure 3b), corresponding to the broad absorption band centered at 16 300 cm^{-1} in the visible spectrum (Figure 3a). The positive features at 14 800 cm^{-1} ($\Delta\epsilon$ = 100 M^{-1} cm^{-1}) and 18 100 cm^{-1} ($\Delta\epsilon$ = 130 M^{-1} cm^{-1}), bands 1 and 3, are less intense than the strong negative feature at 16 300 cm^{-1} ($\Delta\epsilon$ = 170 M^{-1} cm^{-1}), band 2. A weaker positive band, band 4, appears as a shoulder at 21 000 cm^{-1} ($\Delta\epsilon$ = 30 M^{-1} cm^{-1}) on band 3 and is followed by a weak negative feature, band 5, at 22 900 cm^{-1} ($\Delta\epsilon$ = 7 M^{-1} cm^{-1}). Two consecutive weak negative−positive features, bands 6−9, fall in the range 25 700−32 000 cm^{-1} and are followed by a broad negative band, band 10, at 33 300 cm^{-1} ($\Delta\epsilon$ = 80 M^{-1} cm^{-1}) and a broad positive band, band 11, at 36 000 cm^{-1} ($\Delta\epsilon$ = 100 M^{-1} cm^{-1}) (Figure 3b).

---

(68) Baerends, E. J.; Ellis, D. E.; Ros, P. *Chem. Phys.* **1973**, *2*, 41−51.
(69) te Velde, G.; Baerends, E. J. *J. Comput. Phys.* **1992**, *99*, 84−98.
(70) Vosko, S. H.; Wilk, L.; Nusair, M. *Can. J. Phys.* **1980**, *58*, 1200−1211.
(71) Becke, A. D. *Phys. Rev. A.* **1988**, *38*, 3098−3100.
(72) Perdew, J. P. *Phys. Rev. B.* **1986**, *33*, 8822−8824.
(73) Slater, J. C. *Adv. Quantum. Chem.* **1972**, *6*, 1−92.
(74) *Gaussian 94*; Revision E.2 ed.; Gaussian, Inc.: Pittsburgh, PA, 1995.

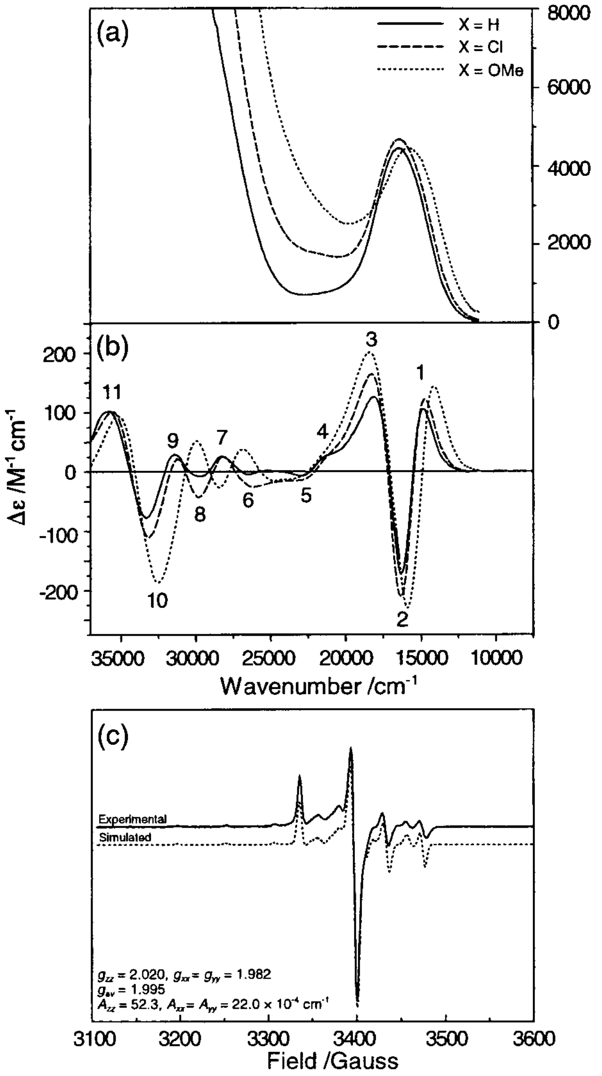

Figure 3. (a) The absorption spectra of $[PPh_4][MoO(p\text{-}SC_6H_4X)_4]$ (X = H, Cl, OMe) in CH_2Cl_2 solution at 298 K. (b) The MCD spectra of $[PPh_4][MoO(p\text{-}SC_6H_4X)_4]$ (X = H, Cl, OMe) in 1,2-dichloroethane/DMF (1:1) frozen glass solution at 5 T, 4.2 K. The numbering of the bands refers to the MCD spectrum of $[PPh_4][MoO(p\text{-}SC_6H_4X)_4]$ (X = H). Deconvolution of the region below 25 000 cm^{-1} appears in Figure 9. (c) The 1,2-dichloroethane/DMF (1:1) frozen glass solution X-band spectrum of $[PPh_4][MoO(p\text{-}SC_6H_4X)_4]$ (X = H) at 77 K. A simulated spectrum, together with the spin Hamiltonian parameters, is shown below the experimental spectrum.

The room-temperature CH_2Cl_2 solution spectra of $[PPh_4][MoO(p\text{-}SC_6H_4X)_4]$ (X = H, Cl, OMe) (Figure 3a) show a small shift in the low-energy absorption (X = H, 16 300 cm^{-1}; X = Cl, 16 400 cm^{-1}; X = OMe, 15 600 cm^{-1}) and a progressively earlier onset of the intense high-energy bands. The 1,2-dichloroethane/DMF (1:1) frozen glass MCD spectra of $[PPh_4][MoO(p\text{-}SC_6H_4X)_4]$ (X = H, Cl, OMe) from 37 000 to 11 700 cm^{-1} exhibit similar behavior (Figure 3b). However, for X = OMe, there are appreciable shifts (600−800 cm^{-1}) to lower energies for bands 6−11 with respect to the X = H, Cl spectra.

The frozen 1,2-dichloroethane/DMF (1:1) solution X-band EPR spectrum of $[PPh_4][MoO(SPh)_4]$ recorded at 77 K is shown in Figure 3c. Simulation[67] of the EPR spectrum reveals an axial spectrum with $g_{\|} = 2.020$, $g_{\perp} = 1.982$, $A_{\|} = 52.3$, and $A_{\perp} = 22.0 \times 10^{-4}$ cm^{-1}. The X-band EPR spectra of $[PPh_4][MoO(p\text{-}SC_6H_4X)_4]$ (X = Cl, OMe) (not shown) are indistinguishable from that of $[PPh_4][MoO(SPh)_4]$.

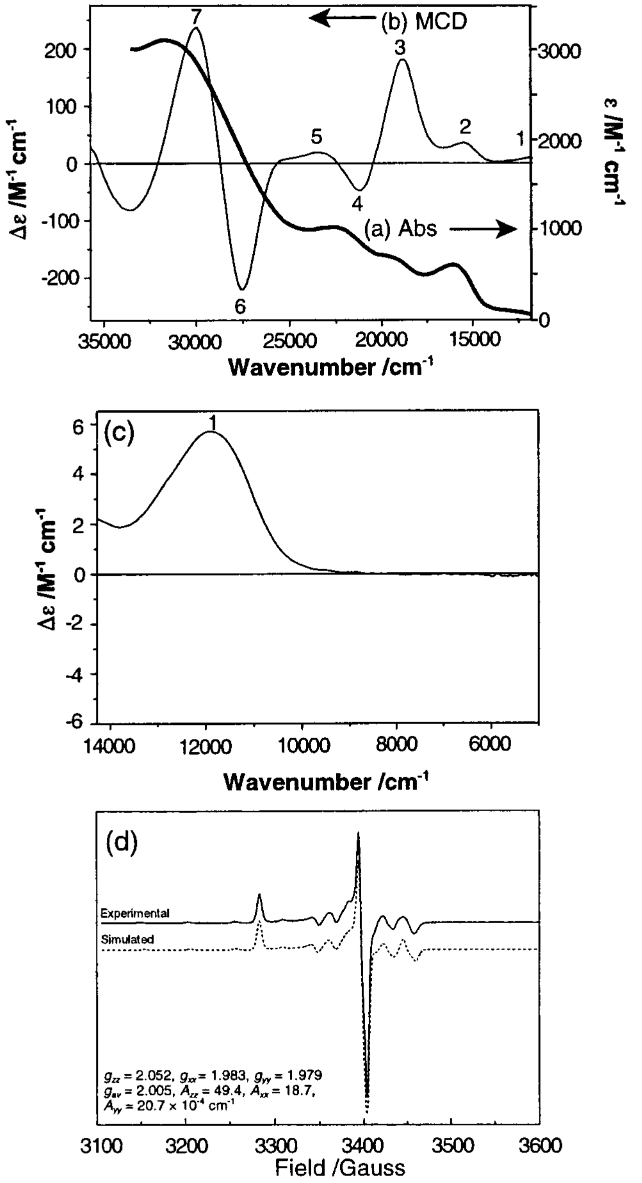

Figure 4. (a) The absorption spectrum of $[PPh_4][MoO(edt)_2]$ in CH_2Cl_2 solution at 298 K. The MCD spectrum of $[PPh_4][MoO(edt)_2]$ in 1,2-dichloroethane/DMF (1:1) frozen glass solution at 5 T, 4.2 K (b) between 33 000 and 12 000 cm^{-1} and (c) between 14 300 and 5000 cm^{-1}. Deconvolution of the region below 25 000 cm^{-1} appears in Figure 10. (d) The 1,2-dichloroethane/DMF (1:1) frozen glass solution X-band spectrum of $[PPh_4][MoO(edt)_2]$ at 77 K. A simulated spectrum, together with the spin Hamiltonian parameters, is shown below the experimental spectrum.

B. $[PPh_4][MoO(edt)_2]$. The room-temperature CH_2Cl_2 solution absorption spectrum and the 1,2-dichloroethane/DMF (1:1) frozen glass MCD spectrum at 4.2 K and 5 T of $[PPh_4][MoO(edt)_2]$ from 33 000 to 12 000 cm^{-1} are shown in Figure 4a,b, and the 1,2-dichloroethane/DMF (1:1) frozen glass MCD spectrum at 4.2 K and 5 T from 14 300 to 5000 cm^{-1} is shown in Figure 4c. The energies, the numbering of the MCD bands, and the energies and f_{exptl} from a Gaussian deconvolution of the room-temperature CH_2Cl_2 solution absorption spectrum (see below, Figure 12) are presented in Table 2. The rich MCD spectrum shows a temperature and field dependence indicative of *C* terms arising from an approximately $g = 2.0$ species.[29] The lowest energy band (band 1) in the MCD spectrum occurs at 11 900 cm^{-1} ($\Delta\epsilon \approx 6$ M^{-1} cm^{-1}, Figure 4c), which corresponds to a weak feature in the absorption spectrum at

Table 2. Solution Absorption and Frozen Glass MCD Spectral Data for $[PPh_4][MoO(edt)_2]$

band number[a]	energy/cm^{-1} MCD[b]	energy/cm^{-1} UV/vis[c]	f_{exptl}	assignments[a,b]
1	11 900 (+)	13 400	0.001	$b_2(\pi) \rightarrow a_1(d_{x^2-y^2})$ (+)
2	15 400 (+)	15 600	0.004	b_2(pseudo-σ) $\rightarrow a_1(d_{x^2-y^2})$ (+)
		16 900	0.003	b_1(pseudo-σ) $\rightarrow a_1(d_{x^2-y^2})$ (−) $a_1(d_{x^2-y^2}) \rightarrow b_2(d_{yz})$ (+)
3	18 800 (+)	18 900	0.005	a_1(pseudo-σ) $\rightarrow a_1(d_{x^2-y^2})$ (+)
4	21 200 (−)	21 200	0.007	$b_{1,2}(\pi) \rightarrow b_{1,2}(d_{xz,yz})$ (−)
5	23 500 (+)	23 500	0.016	$b_{1,2}(\pi) \rightarrow b_{1,2}(d_{xz,yz})$ (+)
6	27 600 (−)			$a_{1,2}(\pi) \rightarrow b_{1,2}(d_{xz,yz})$ (+)
7	29 900 (+)			$a_{1,2}(\pi) \rightarrow b_{1,2}(d_{xz,yz})$ (−)

[a] The band numbering refers to features in the MCD spectrum of $[PPh_4][MoO(edt)_2]$ (Figure 4). [b] 1,2-dichloroethane/DMF (1:1) frozen glass solution, 5 T, 4.2 K; the signs of the MCD transitions are given in parentheses. [c] CH_2Cl_2 solution, 298 K

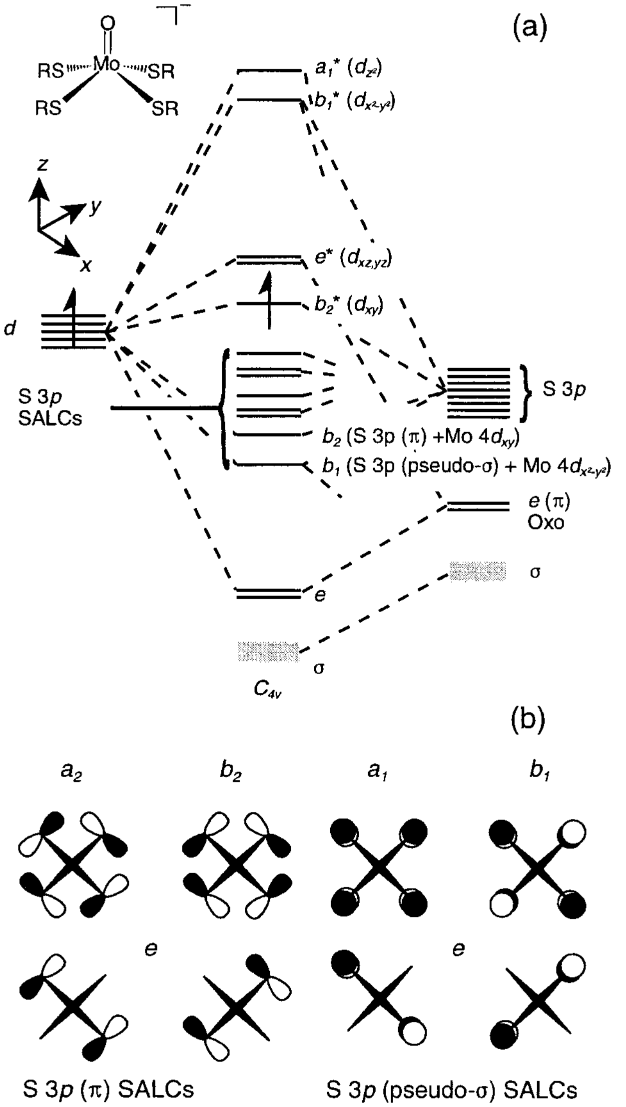

Figure 5. (a) A qualitative molecular orbital diagram for $[MoO(SMe)_4]^-$ in C_{4v} symmetry corresponding to a O−Mo−S−C(α) dihedral angle of 0° (Figure 2c). (b) The symmetry adapted linear combinations (SALCs) of the S 3p (π) and 3p(pseudo-σ) orbitals in C_{4v} symmetry; see also Figure 2d,e.

approximately 12 800 cm^{-1} (Figure 4a). The weak intensity of this band in the absorption spectrum made an estimation of its absorbance maximum difficult, and it is likely that the energy of the corresponding MCD band is more reliable. The first strong absorption in the visible spectrum occurs at 15 900 cm^{-1} (ϵ = 600 M^{-1} cm^{-1}) and corresponds to the positive feature in the MCD spectrum, band 2, at 15 400 cm^{-1} ($\Delta\epsilon$ = 40 M^{-1} cm^{-1}). Bands 3 and 4 in the MCD spectrum, 18 800 cm^{-1}($\Delta\epsilon$ = 180 M^{-1} cm^{-1}) and 21 200 cm^{-1} ($\Delta\epsilon$ = −50 M^{-1} cm^{-1}), respectively, are contained in the absorption at 20 000 cm^{-1} (ϵ = 720 M^{-1} cm^{-1}, Figure 4a). Band 5 at 23 500 cm^{-1} ($\Delta\epsilon$ = 19 M^{-1} cm^{-1}) occurs at the same energy as the third low energy band, 23 500 cm^{-1} (ϵ = 1000 M^{-1} cm^{-1}) in the visible spectrum (Figure 4a). The strong negative−positive features in the MCD spectrum of $[PPh_4][MoO(edt)_2]$, bands 6 and 7, occur at 27 600 cm^{-1} ($\Delta\epsilon$ = −220 M^{-1} cm^{-1}) and 29 900 cm^{-1} ($\Delta\epsilon$ = 240 M^{-1} cm^{-1}) and lie under the intense absorption with a band maximum at 31 600 cm^{-1} (ϵ = 3100 M^{-1} cm^{-1}) in the UV/vis spectrum (Figure 4a).

The frozen 1,2-dichloroethane/DMF (1:1) solution X-band EPR spectra of $[PPh_4][MoO(edt)_2]$ recorded at 77 K is shown in Figure 4d. Simulation of the EPR spectrum reveals an slightly rhombic spectrum with $g_{zz} = 2.052$, $g_{xx} = 1.983$, $g_{yy} = 1.979$, $A_{zz} = 49.4$, $A_{xx} = 18.7$, and $A_{yy} = 20.7 \times 10^{-4}$ cm^{-1}.

2. Molecular Orbital Calculations. A. $[PPh_4][MoO(\textit{p}\text{-}SC_6H_4X)_4]$ (X = H, Cl, OMe). A qualitative molecular orbital diagram for $[MoOS_4]^-$ in C_{4v}, derived from that of $[MoOCl_4]^-$ [41,45] and group theory, is shown in Figure 5. The strong σ and π donor properties of the axial oxo ligand destabilize the $4d_{z^2}$ and the $4d_{xz}/4d_{yz}$ orbitals within the d orbital manifold. The electronic configuration for Mo in $[MoOS_4]^-$ is formally $4d^1$, and this unpaired electron resides in the $4d_{xy}$ orbital to give a doublet ground state. Beneath this d orbital manifold there are a set of eight orbitals corresponding to SALCs of the S ligand 3p lone pairs (Figure 5b). The four remaining S 3p orbitals involved in σ bonding to the C(α) of the thiolate ligand are directed away from the metal center and are at deep binding energy relative to the Mo 4d orbitals. Four of the S 3p orbitals in Figure 5b form SALCs of π symmetry with respect to the Mo center and lie in the plane containing the four S atoms. On the basis of the geometry of $[MoO(SPh)_4]^-$ (O−Mo−S = 109.9°, Mo−S−C = 109.8°), the remaining four S lone pair orbitals form pseudo-σ bonding SALCs with respect to Mo and are directed along the Mo−S bonds toward the Mo atom (Figure 2d,e).

The O−Mo−S−C(α) dihedral angle plays an important role in determining the orientation of the S lone pairs with respect to the Mo 4d orbitals. An assessment of the effect of this angle on the energies of the frontier orbitals was made using DFT calculations on the $[MoO(SMe)_4]^-$ model (Figure 2b,c). The results of varying the dihedral angle between 0° (C_{4v}) and 90° (C_4) in a clockwise sense for all four ligands are shown in the Walsh diagram (Figure 6a). There are large changes in the energies of the S lone pair orbitals of π symmetry, whereas those of pseudo-σ symmetry with respect to Mo show a smaller variation in energy because their electron density is directed principally along the Mo−S bond. Rotation about the S−Mo axes causes the S π orbitals to rotate out of the 4 S plane and breaks the strong bonding−antibonding interaction between the $4d_{xy}(b_2)$ and S $\pi(b_2)$ (Figure 6a). The Walsh diagram (Figure 6a) shows that the energies of these bonding and antibonding components are highly dependent on the O−Mo−S−C(α) dihedral angle, and the interaction between them is minimized at a O−Mo−S−C(α) dihedral angle of 90°, where the S π orbitals are orthogonal to $4d_{xy}$ and parallel to the Mo≡O bond. Figure 7 shows the calculated contour plots for the HOMO for three different dihedral angles. The rotation also permits π(e) participation in the Mo≡O bond through overlap with the $4d_{xz}/4d_{yz}$ orbitals, which increases as O−Mo−S−C(α) increases

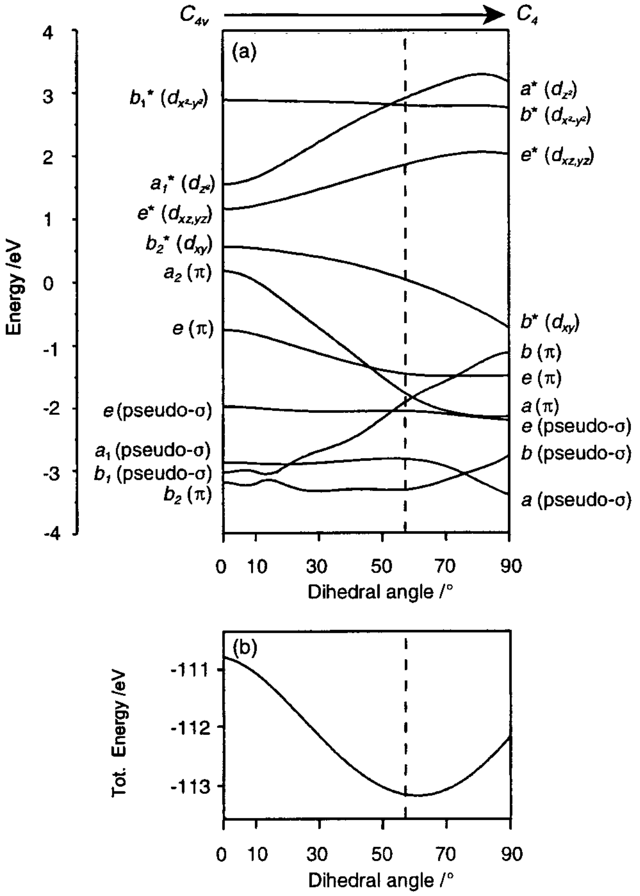

Figure 6. A Walsh diagram, derived from DFT calculations, showing (a) the variation in the energy of the frontier orbitals and (b) the total energy of $[MoO(SMe)_4]^-$ with O−Mo−S−C(α) dihedral angle. O−Mo−S−C(α) varies between 0° (C_{4v}) and 90° (C_4) in the sense shown in Figure 2c. The dotted line indicates the average X-ray crystallographic O−Mo−S−C(α) dihedral angle (58.8°) for $[MoO(SPh)_4]^-$.

(Figure 6). In addition, the $4d_{z^2}$ orbital is strongly destabilized as the dihedral angle increases from 0° to 90°, due to an interaction with the S $\pi(a_2)$ orbital that becomes allowed in C_4 symmetry. The $4d_{x^2-y^2}$ orbital points toward the nodes in the π SALCs at all O−Mo−S−C(α) dihedral angles and remains essentially unaffected in energy as the S π orbitals rotate.

The total bonding energy in $[MoO(SMe)_4]^-$ is maximized at a dihedral angle of 62.8° (Figure 6b), which is comparable to the angle observed experimentally in $[MoO(SPh)_4]^-$ (58.8°), where repulsions between the S 3p lone pair orbitals are minimized. The energies of the frontier orbitals in $[MoO(SPh)_4]^-$ at O−Mo−S−C(α) = 58.8° from spin restricted and unrestricted calculations are shown in Figure 8. In both calculations the energy order of the S lone pair and Mo 4d orbitals is retained. The Mo 4d, S 3p, and O 2p compositions of the frontier orbitals for a spin restricted DFT calculation on $[MoO(SMe)_4]^-$ at O−Mo−S−C(α) = 58.8° are shown in Table 3 and support considerable Mo−S mixing. The HOMO, the singly occupied 17a orbital (Figure 8), is 53.0% Mo $4d_{xy}$ and 35.4% total S 3p character; the LUMO (17b/18b*)* is 55.5% Mo $4d_{xz,yz}$ and 16.8% total S 3p character.

B. $[PPh_4][MoO(edt)_2]$. Qualitatively, the molecular orbital diagram of $[MoO(edt)_2]^-$ in C_{2v} symmetry (Figure 9a) might be expected to be similar to those for $[MoOCl_4]^-$,[41,45] and $[MoOS_4]^-$ in C_4 (Figure 6a, dihedral angle = 90°). Note that for C_{2v} symmetry the coordinate system is rotated by 45° such that in $[MoO(edt)_2]^-$ the singly occupied orbital that corresponds to Mo $4d_{xy}$ in Figure 6 becomes Mo $4d_{x^2-y^2}$ in Figure 9a. The Walsh diagram (Figure 6a) suggests that the energy separation between this singly occupied Mo 4d orbital, which lies between the ligands in the equatorial plane, and the highest occupied Sπ SALC of $[MoO(edt)_2]^-$, should be substantially less than the analogous separation in $[MoOS_4]^-$ at its equilibrium geometry. The eight SALCs derived from the S 3p orbitals and their symmetries are shown in Figure 9b. In contrast to the monodentate p-$SC_6H_4X^-$ (X = H, Cl, OMe) ligands, the rigid C−C backbone of edt^{2-} orients the π SALCs parallel to the Mo≡O with those of b_1 and b_2 symmetry possessing orbital overlap properties that are appropriate for participation in the Mo≡O bond. The stabilization of the pseudo-σ orbitals, through interactions with the Mo 4d orbitals, places them beneath the S π orbitals. The pseudo-σ a_2 SALC interacts strongly with the Mo $4d_{xy}$ orbital, and the pseudo-σ a_1 SALC can interact with the Mo $4d_{x^2-y^2}$ orbital (a similar interaction between benzenedithiolate and Mo has been inferred from absorbance, MCD, and resonance Raman studies on $(L-N_3)MoO(bdt)$.)[54] The average O−Mo−S angle (105.9°) in $[MoO(edt)_2]^-$ permits the overlap of the b_1 and b_2 pseudo-σ orbitals with Mo $4d_{xz}$ and $4d_{yz}$, respectively, which points to their potential involvement in modulating the strength of the Mo≡O bond.

Spin restricted and unrestricted DFT calculations on a $[MoO(edt)_2]^-$ model using molecular parameters from the X-ray crystal structure of $[MoO(edt)_2]^-$,[56] idealized to C_{2v} symmetry, reveal that the S π orbitals are of similar energy to the Mo 4d manifold (as qualitatively suggested from Figure 6a as the dihedral angle increases from 58° to 90°). The spin restricted calculation places the occupied S $6a_2$ SALC *above* the singly occupied Mo $4d_{x^2-y^2}$ ($10a_1$) (Figure 10). The spin unrestricted DFT calculation also supports a mixed level[75] description of the bonding in $[MoO(edt)_2]^-$ in which six ligand-based S π orbitals ($6a_2$ $\alpha\beta$, $7b_1$ $\alpha\beta$, and $8b_2$ $\alpha\beta$) lie above the highest occupied metal-based orbital ($10a_1$ α) (Figure 10). This mixed level scheme results from spin polarization and the close spacing of the metal and ligand levels, a consequence of the increase in energy of the S π orbitals due to the increased repulsion between the S lone pairs induced by the rigid geometry imposed by the C−C backbone of edt^{2-} (Figure 6a).

The compositions of the α and β spin orbitals, Tables 4 and S3, respectively, show considerable Mo−S covalency within the d orbital manifold in $[MoO(edt)_2]^-$. In particular, for the α spin orbitals the total S p orbital character (21.9%) in the $9b_2$ (Mo $4d_{yz}$) orbital slightly exceeds that of the oxo contribution (20.6%). For $8b_1$ (Mo $4d_{xz}$) the total S p character (18.7%) and the oxo contribution (21.6%) are also similar. However, the $10a_1$ α orbital is 71.4% Mo $4d_{x^2-y^2}$ and the LUMO, 10 a_1 β (Table S3), is 74% Mo $4d_{x^2-y^2}$. This is much less covalent than the corresponding 17a orbital calculated for $[MoO(SCH_3)_4]^-$ (Figure 8), which is 53.0% Mo $4d_{xy}$. These covalency differences in the lowest lying acceptor orbitals for the two compounds derive from the fact that the $8a_1$ (pseudo-σ) orbital in $[MoO(edt)_2]^-$ is at lower energy than the b(π) [15a] orbital in $[MoO(SCH_3)_4]^-$ (Tables 3 and 4). The substantially greater absorption intensity of the low-energy LMCT bands for $[MoO(SPh)_4]^-$ (Figure 3) compared to $[MoO(edt)_2]^-$ (Figure 4) is consistent with the calculated covalency differences of the LUMOs for these two types of compounds (Tables 3 and S3).

3. Selection Rules and Band Assignments. A. $[PPh_4][MoO(p$-$SC_6H_4X)_4]$ (X = H, Cl, OMe). For a randomly oriented

---

(75) Noodleman, L.; Peng, C. Y.; Case, D. A.; Mouesca, J.-M. *Coord. Chem. Rev.* **1995**, *114*, 199−244.

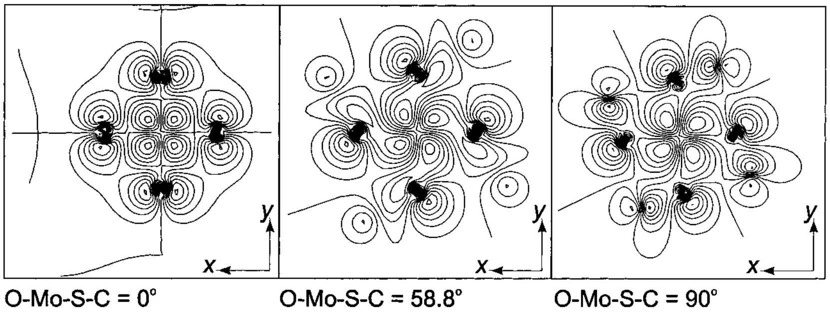

Figure 7. DFT calculation contour plot of the highest occupied molecular orbital (HOMO) of $[MoO(SMe)_4]^-$ at O−Mo−S−C(α) dihedral angles of 0°, 58.8°, and 90°.

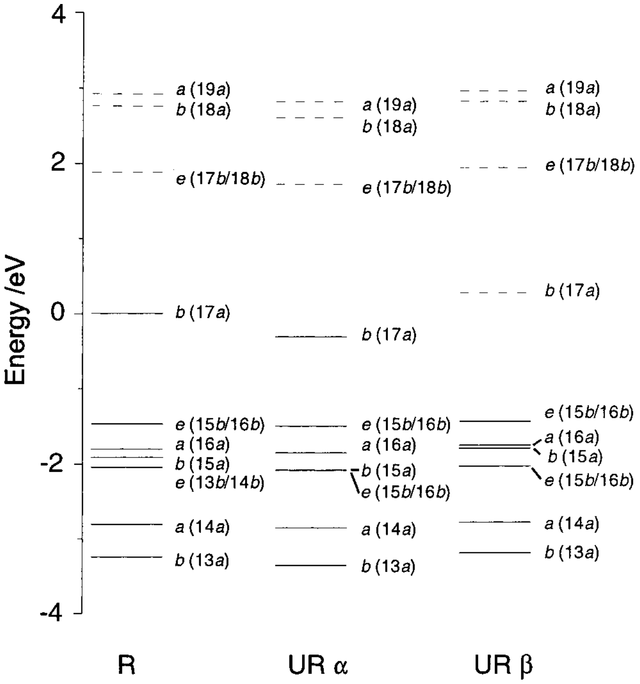

Figure 8. Energies of the frontier orbitals of $[MoO(SMe)_4]^-$ derived from spin restricted (R) and unrestricted (UR) DFT calculations. Occupied orbitals are shown with solid lines and unoccupied orbitals are shown with dotted lines.

molecule the intensity of a C-term transition is given by[27−29,76]

$$C_0 = -\frac{i}{3|A|}\sum_{\alpha\alpha'\lambda}\langle A\alpha'|(\mathbf{L}+2\mathbf{S})|A\alpha\rangle\cdot(\langle A\alpha|\mathbf{m}|J\lambda\rangle\,\langle J\lambda|\mathbf{m}|A\alpha'\rangle) \tag{1}$$

where A and J represent the spin−orbit corrected ground and excited states, respectively, $\mathbf{L}+2\mathbf{S}$ is the Zeeman operator, $\mathbf{m}$ is the transition moment operator, $|A|$ denotes the degeneracy of A (equal to 2 for Mo(V)), and the sum is over components of the Kramers doublet in the ground (α, α') and excited (λ) states. With respect to MCD in C_{4v} symmetry, three different types of transitions may be identified, two of which require spin−orbit coupling for nonzero C term intensity. First, the transition can be to a degenerate state of e symmetry which is x,y polarized in absorption. Spin−orbit coupling within the e manifold splits the degenerate pair by an amount λ, where λ is the net spin−orbit coupling constant of the delocalized final state. In C'_{4v}, e splits into Γ_7 and Γ_6 with $|m_J| = 3/2$ and 1/2, respectively, while the b_2 ground-state transforms as Γ_7 with $|m_J| = 1/2$.[77] At low temperature and high field only the $m_J = -1/2$ component of the ground-state Kramers doublet will be populated. The MCD selection rules are $\Delta m_S = 0$ and $\Delta m_J = \pm1$ for positive or negative MCD sign, which imply that the $\Gamma_7(d_{xy}) \rightarrow \Gamma_7(e)$ transition will exhibit a positive C term, while the $\Gamma_7(d_{xy}) \rightarrow \Gamma_6(e)$ transition will exhibit a negative C term. For cases where this splitting is less than the instrument bandwidth, the two components will overlap, giving rise to a derivative shaped pseudo-A term. A positive pseudo-A term results for transitions to a metal-based E term, where the *positive* sign of the spin−orbit coupling constant requires the Γ_7 component to be higher in energy than the Γ_6 component in C'_{4v} symmetry, split from each other approximately by the spin−orbit coupling constant, $\xi_{3d}(\mathrm{Mo(V)}) \approx 900\ \mathrm{cm}^{-1}$.[78] For transitions from a ligand-based E term the *negative* value of the spin−orbit coupling constant results in a negative pseudo-A term with the negative feature to higher energy than the positive feature, since the Γ_6 component now lies to higher energy than the Γ_7 component. The positive and negative features are split approximately by the spin−orbit coupling constant, $\xi_{3p}(\mathrm{S}) \approx 374\ \mathrm{cm}^{-1}$.[79]

A second class of transitions in C_{4v} includes transitions from $^2B_2$ to $^2B_1$, $^2A_1$, and $^2A_2$ that are group theoretically forbidden in absorption. For MCD transitions between these nondegenerate states, $\langle A\alpha|\mathbf{m}|J\lambda\rangle$ in eq 1 is zero[76] and no C-term intensity is expected. However, in C'_{4v}, out-of-state spin−orbit coupling with the fully allowed E states mixes some x, y character into the forbidden states. In C'_{4v} $^2A_1$ and $^2A_2$ transform as Γ_6 and give rise to negative C-terms, whereas $^2B_1$ transforms as Γ_7 and gives rise to positive C-term intensity.

The final class corresponds to $^2B_2 \leftarrow {}^2B_2$ transitions that are allowed in z polarization. However, eq 1 requires $\langle A\alpha|m_i|J\lambda\rangle$ ($i = x, y, z$) to be nonzero for at least two values of i for C-term intensity, and consequently, in the absence of spin−orbit coupling, $^2B_2 \leftarrow {}^2B_2$ transitions exhibit no C-term intensity. The inclusion of spin−orbit coupling leads to $^2B_2 \leftarrow {}^2B_2$ transitions being of positive sign.

The Walsh diagram (Figure 6) enables a correlation between orbitals in C_{4v} symmetry with those in C_4, permitting the derivation of the absorption and MCD selection rules through desent in symmetry for $[MoO(SMe)_4]^-$. Thus, $^2E \leftarrow {}^2B$ transitions are x, y polarized, giving rise to positive pseudo-A terms for transitions that are metal centered and negative pseudo-A terms

---

(76) Gerstman, B. S.; Brill, A. S. *J. Chem. Phys.* **1985**, *82*, 1212−1230.

(77) Koster, G. F.; Dimmock, J. O.; Wheeler, R. G.; Statz, H. *Properties of the Thirty-Two Point Groups*; M. I. T. Press: Cambridge, Massachusetts, 1963.

(78) Figgis, B. N. In *Introduction to Ligand Fields*; John Wiley & Sons Inc: New York, 1966.

(79) Mabbs, F. E.; Collison, D. In *Electronic Paramagnetic Resonance of d Transtion Metal Compounds*; Elsevier: Amsterdam, 1992.

Table 3. Results of DFT Calculations for the Frontier Orbitals of $[MoO(SMe)_4]^-$ [a]

molecular orbital symmetry[a]			composition/%										
			Mo					O			S		
C_4	C_2	energy/eV	$4d_{z^2}$	$4d_{x^2-y^2}$	$4d_{xy}$	$4d_{xz}$	$4d_{yz}$	$2p_x$	$2p_y$	$2p_z$	$3p_x$	$3p_y$	$3p_z$
b(pseudo-σ)	[13a]	−2.988	0.0	25.6	4.9	0.0	0.0	0.0	0.0	0.0	17.7	17.7	17.1
a(pseudo-σ)	[14a]	−2.561	2.4	0.0	0.0	0.0	0.0	0.0	0.0	5.3	19.8	19.8	29.4
e(pseudo-σ)	[13b]	−1.789	0.0	0.0	0.0	0.0	4.5	0.0	7.9	0.0	16.8	50.5	9.9
	[14b]	−1.789	0.0	0.0	0.0	4.5	0.0	7.9	0.0	0.0	50.5	16.8	9.9
b(π)	[15a]	−1.659	0.0	0.7	26.3	0.0	0.0	0.0	0.0	0.0	5.6	5.6	44.3
a(π)	[16a]	−1.549	2.1	0.0	0.0	0.0	0.0	0.0	0.0	4.9	21.5	21.5	38.2
e(π)	[15b]	−1.213	0.0	0.0	0.0	0.0	1.8	0.1	2.8	0.0	15.4	0.0	71.7
	[16b]	−1.213	0.0	0.0	0.0	1.8	0.0	2.8	0.1	0.0	0.0	15.4	71.7
b($4d_{xy}$)	**[17a]**	**0.000**	**0.0**	**0.8**	**53.0**	**0.0**	**0.0**	**0.0**	**0.0**	**0.0**	**10.7**	**10.7**	**14.0**
e($4d_{xz,yz}$)	[17b]	1.875	0.0	0.0	0.0	0.2	55.5	0.1	19.8	0.0	4.5	9.3	0.3
	[18b]	1.875	0.0	0.0	0.0	55.5	0.2	19.8	0.1	0.0	9.3	4.5	0.3
b($4d_{x^2-y^2}$)	[18a]	2.759	0.0	45.3	0.1	0.0	0.0	0.0	0.0	0.0	13.3	13.3	9.1
a($4dz^2$)	[19a]	2.921	28.7	0.0	0.0	0.0	0.0	0.0	0.0	15.9	4.6	4.6	6.0

[a] The calculations were carried out in C_2 symmetry with effective C_4 symmetry. The symmetry labels for both symmetries are shown. The highest occupied molecular orbital (HOMO) is shown in bold.

for LMCT transitions. $^2A \leftarrow ^2B$ transitions are forbidden but give rise to negative *C*-terms through spin−orbit coupling, and $^2B \leftarrow ^2B$ transitions are *z* polarized in absorption and become allowed in MCD through spin−orbit coupling to give positive *C*-terms.

Oscillator strengths, f_{calc}, can be calculated from DFT derived wave functions using the ligand−ligand overlap term of van der Avoird and Ross.[80] Using this approach the f_{calc} is approximated as a sum of the overlaps between ligand centered orbitals in the ground (Φ_L) and excited state (Φ_L') molecular orbitals such that

$$f_{calc} = 1.085 \times 10^{11}(\Delta E)|D|^2 \quad (2)$$

in which

$$D = \langle \Phi_L' | \vec{\mathbf{r}} | \Phi_L \rangle \approx \sum_a \sum_b C'_{ab} C_{ab} \vec{\mathbf{r}}_a \quad (3)$$

where ΔE is the transition energy, C_{ab} and C'_{ab} are the coefficients of orbital *b* on ligand *a* for the ground and excited-state molecular orbitals, respectively, and $\vec{\mathbf{r}}$ is the position vector to ligand *a*. Within this approximation eqs 2 and 3 show that in order for a charge-transfer transition to have intensity in absorption, the same type of orbital (S pseudo-σ or S π) must be present on a given ligand in both the ground and excited states. The calculated transition energies and f_{calc} from the eight S 3p SALCs to Mo $4d_{xy}$ in $[MoO(SMe)_4]^-$ are shown in Table 5.

A combination of symmetry arguments, partial Gaussian deconvolution, the calculated transition energies for $[MoO(SMe)_4]^-$, and orbital overlap considerations allows for reasonable simultaneous assignments of the UV/vis and MCD spectra of $[PPh_4][MoO(SPh)_4]$. In addition, the transition energy calculations on $[MoO(SMe)_4]^-$ anticipate significant overlap between the low-energy LMCT and LF bands (Table 5). Thus, given the low oscillator strengths of LF transitions in oxomolybdenum complexes (ϵ < 100 M^{-1} cm^{-1}), LMCT bands are expected to dominate the absorption spectra from 11 700 to 25 000 cm^{-1}.[41]

The room-temperature CH_2Cl_2 solution absorption spectrum of $[PPh_4][MoO(SPh)_4]$ over 11 700−25 000 cm^{-1} was fitted with a minimum number of two symmetric Gaussian functions at 16 300 and 22 350 cm^{-1} (Figure 11a). Oscillator strengths, f_{calc}, derived from DFT calculations on $[MoO(SMe)_4]^-$ suggest that the visible spectrum should be dominated by two absorptions arising from two $^2E \leftarrow ^2B$ LMCT transitions involving the e(π) and e(pseudo-σ) SALCs at calculated energies of 15 900 and 20 100 cm^{-1}, respectively (Table 4). In the MCD spectrum

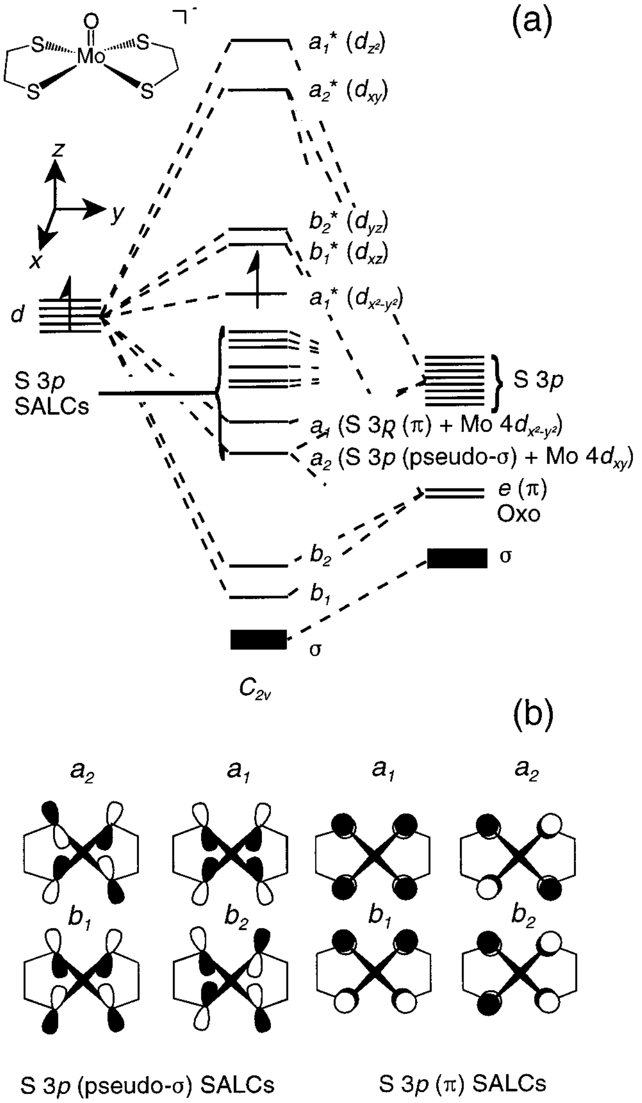

Figure 9. (a) A qualitative molecular orbital diagram for $[MoO(edt)_2]^-$ in C_{2v} symmetry. (b) The symmetry adapted linear combinations (SALCs) of the S 3p(π) and 3p(pseudo-σ) orbitals in C_{2v} symmetry.

---

(80) van der Avoird, A.; Ros, P. *Theor. Chim. Acta* **1966**, *4*, 13-21.

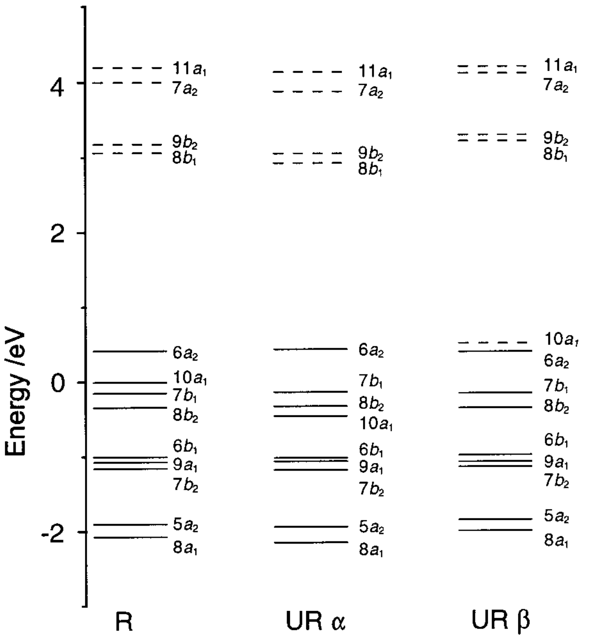

Figure 10. Energies of the frontier orbitals of $[MoO(edt)_2]^-$ derived from spin restricted (R) and unrestricted (UR) DFT calculations. Occupied orbitals are shown with solid lines and unoccupied orbitals are shown with dotted lines.

of $[PPh_4][MoO(SPh)_4]$, these transitions were modeled by negative pseudo-A terms possessing zero MCD intensity at energies corresponding to the absorption maxima at 16 300 and 22 350 cm^{-1}, respectively. The rest of the MCD spectrum from 11 700 to 25 000 cm^{-1} required a minimum of four additional Gaussian functions for a reasonable fit (Figure 11b).

Band 1. Band 1 (Figures 3b and 11b) is the lowest energy transition observed in the MCD spectrum of $[PPh_4][MoO(SPh)_4]$ and is assigned, in part, to $b(\pi)\rightarrow b(d_{xy})$ LMCT. The relatively high positive MCD intensity is consistent with a formally MCD forbidden transition gaining intensity through out-of-state spin−orbit coupling. At the C_{4v} limit, this transition corresponds to LMCT from a $b_2(\pi)-b_2(d_{xy})$ bonding to antibonding orbital, and in C_4, at the crystallographic O−Mo−S−C(α) dihedral angle of 58.8°, the $b(\pi)$ orbital still possesses considerable Mo $4d_{xy}$ character (26.3%, Table 3). In contrast, LMCT from other low-lying S 3p SALCs are less metal-based and are expected to show less MCD enhancement through out-of-state spin−orbit coupling.

Transition energy calculations also place the $e(\pi)\rightarrow b(d_{xy})$ LMCT transition within this energy range at 15 900 cm^{-1} (Table 5). The calculated oscillator strength for this absorption ($f_{calc} = 0.213$, Table 5) suggests that it should dominate the visible spectrum, and the absorption maximum at 16 300 cm^{-1} (Figure 11a) is assigned to this transition. This energy sets the zero absorption for the negative pseudo-*A* transition in the MCD spectrum, and Gaussian fitting places the positive feature of this transition well within the region of band 1 (Figure 11b).

In summary, band 1 is assigned to a positive $b(\pi)\rightarrow b(d_{xy})$ *C*-term and a positive feature of a negative pseudo-*A* term resulting from the fully allowed $e(\pi)\rightarrow b(d_{xy})$ transition. An alternative assignment has been proposed by McNaughton et al.[64] Their analysis of the spectra yields assignments for bands 1 and 2 that are the reverse of ours.

Bands 2 and 3. These bands constitute a positive pseudo-*A* feature centered at 17 000 cm^{-1} (Figure 11b) and is easily identifiable as a $b(d_{xy})\rightarrow e(d_{xz,yz})$ LF transition that is fully allowed in MCD.[41] This transition occurs at 16 000 cm^{-1} and at 15 800 cm^{-1} in $[MoOCl_4]^-$[41] and $(L-N_3)MoO(bdt)$, respectively.[54] Within the series $[PPh_4][MoO(p\text{-}SC_6H_4X)_4]$ (X = H, Cl, OMe) band 3 remains invariant, which lends support to the $b(d_{xy})\rightarrow e(d_{xz,yz})$ LF assignment because the energy of this transition is determined by the relative energies of the Mo $4d_{xy}$ and $4d_{xz,yz}$ orbitals rather than by the relative energies between the S lone-pair orbitals and the ligand field.

The asymmetric nature of this transition may result from out-of-state spin−orbit coupling that, in the limit of negligible coupling to the ground state, results in the reapportioning of intensity via the sum rule.[76] In addition, overlap with the negative component of the $e(\pi)\rightarrow b(d_{xy})$ pseudo-*A* transition may contribute to the asymmetry of bands 2 and 3.

The $b(d_{xy})\rightarrow e(d_{xz,yz})$ LF absorption is obscured by more intense LMCT transitions in the visible spectrum of $[PPh_4][MoO(SPh)_4]$ and lies within the intense low-energy absorption envelope (Figure 11a). McNaughton et al. have assigned band 3 to a S to d_{xy} charge-transfer transition, but they note that $b(d_{xy})\rightarrow e(d_{xz,yz})$ should also occur in this energy region.[63]

Bands 4 and 5. These bands arise from a negative pseudo-*A* term that results from a MCD-allowed $e(\text{pseudo-}\sigma)\rightarrow b(d_{xy})$ transition centered at 22 350 cm^{-1} with significant absorption intensity (Table 1). An additional positive band, at 19 200 cm^{-1}, was also required for a satisfactory fit of the MCD spectrum (Figure 11b). This is assigned to the $b(d_{xy})\rightarrow b(d_{x^2-y^2})$ LF transition that gains MCD intensity through out-of-state spin−orbit coupling. This band has been identified in the MCD spectrum of $[MoOCl_4]^-$ at 23 000 cm^{-1} but possesses low intensity in absorption.[41] It has been noted that in parent C_{4v} symmetry this transition is orbitally forbidden and that there are no low-lying LMCT transitions that provide an intensity borrowing mechanism.[54] Thus, it is likely that this band is totally obscured by the more intense $e(\text{pseudo-}\sigma)\rightarrow b(d_{xy})$ feature in the visible spectrum.

Bands 6 and 7. Bands 6 and 7 are well-resolved in the MCD spectrum of $[PPh_4][MoO(SPh)_4]$ (Figure 3b) but are obscured by the intense absorption that onsets at approximately 25 000 cm^{-1} in the visible spectrum of $[PPh_4][MoO(SPh)_4]$ (Figure 3a), and consequently the bands were assigned on the basis of a comparison with the transition energy calculations for $[MoO(SMe)_4]^-$ (Table 5). Bands 6 and 7 are assigned to $a(\text{pseudo-}\sigma)\rightarrow b(d_{xy})$ and $b(\text{pseudo-}\sigma)\rightarrow b(d_{xy})$ transitions of negative and positive signs, respectively.

Bands 8 and 9. These weak positive−negative features result from transitions from the ^2B ground state to the ^2B and ^2A excited states derived from an $e(\pi)^1\ b(d_{xy})^1\ e(d_{xz,yz})^1$ electronic configuration. This transition corresponds to $e(\pi)\rightarrow e^*(d_{xz,yz})$ LMCT in the molecular orbital diagram (Figure 5).

Bands 10 and 11. These are easily identifiable as an $a(\pi)$ or $b(\pi)\rightarrow e(d_{xz,yz})$ transition due to their positive pseudo-A character. Both transitions appear reasonable on the basis of transition energy calculations for $[MoO(SMe)_4]^-$ (Table 5) and bands 10 and 11 may result from the overlap of two pseudo-A terms that result from two LMCT transitions from the $a(\pi)$ and $b(\pi)$ SALCs.

In summary, we have been able to provide reasonable assignments for the low-energy bands in the visible and MCD spectra of $[PPh_4][MoO(p\text{-}X\text{-}C_6H_4\text{-}S)_4]$ (X = H, Cl, OMe) (Table 1). We were unable to assign the $a(\pi)\rightarrow b(d_{xy})$ transition that while forbidden in absorption may become allowed in MCD through out-of-state spin−orbit coupling. The DFT calculations place this transition at 16 800 cm^{-1} (Table 5); if this band is present in the MCD spectrum of $[PPh_4][MoO(p\text{-}X\text{-}C_6H_4\text{-}S)_4]$ (X = H), then it likely lies under bands 1−3.

Table 4. Results of Unrestricted DFT Calculations for the Frontier Orbitals of $[MoO(edt)_2]^-$ [a]

molecular orbital symmetry		composition/%										
		Mo					O			S		
C_{2v}	energy/eV	$4d_{z^2}$	$4d_{x^2-y^2}$	$4d_{xy}$	$4d_{xz}$	$4d_{yz}$	$2p_x$	$2p_y$	$2p_z$	$3p_x$	$3p_y$	$3p_z$
$8a_1$(pseudo-σ)	−2.593	1.4	10.24	0.0	0.0	0.0	0.0	0.0	5.2	48.4	4.6	8.5
$5a_2$(pseudo-σ)	−2.378	0.0	0.0	9.5	0.0	0.0	0.0	0.0	0.0	62.4	1.9	0.5
$7b_2$(pseudo-σ)	−1.615	0.0	0.0	0.0	0.0	4.4	0.0	14.9	0.0	56.6	12.0	3.4
$9a_1(\pi)$	−1.499	2.2	0.2	0.0	0.0	0.0	0.0	0.0	7.7	10.3	10.0	62.2
$6b_1$(pseudo-σ)	−1.453	0.0	0.0	0.0	3.6	0.0	14.1	0.0	0.0	66.1	13.6	0.5
$10a_1(4d_{x^2-y^2})$	−0.895	0.4	71.4	0.0	0.0	0.0	0.0	0.0	0.8	5.0	0.1	2.2
$8b_2(\pi)$	−0.763	0.0	0.0	0.0	0.0	2.2	0	7.2	0.0	0.0	2.5	83.2
$7b_1(\pi)$	−0.574	0.0	0.0	0.0	2.1	0.0	5.1	0.0	0.0	1.1	0.2	81.9
$6a_2(\pi)$	**0.000**	**0.0**	**0.0**	**1.1**	**0.0**	**0.0**	**0.0**	**0.0**	**0.0**	**5.1**	**14.8**	**69.4**
$8b_1(4d_{xz})$	2.495	0.0	0.0	0.0	52.2	0.0	21.6	0.0	0.0	6.0	10.0	2.7
$9b_2(4d_{yz})$	2.622	0.0	0.0	0.0	0.0	51.4	0.0	20.6	0.0	11.3	8.0	2.6
$7a_2(4d_{xy})$	3.449	0.0	0.0	41.9	0.0	0.0	0.0	0.0	0.0	12.4	17.9	9.4
$11a_1(4d_{z^2})$	3.170	27.4	0.5	0.0	0.0	0.0	0.0	0.0	13.1	3.6	0.4	8.7

[a] The compositions and energies are for the α spin orbitals. The highest occupied molecular orbital (HOMO) is shown in bold. The compositions and energies of the β spin−orbitals are given in Table S3.

Table 5. Calculated Transition Energies and Oscillator Strengths for $[MoO(SMe)_4]^-$ in C_4 Symmetry[a]

transition[a]	calculated energy/cm^{-1}	f_{calc}[b]
$e(\pi)[15b/16b] \rightarrow b[17a]$	15 900	0.213
$a(\pi)[16a] \rightarrow b[17a]$	16 800	0
$b(\pi)[15a] \rightarrow b[17a]$	16 600	0.024
e(pseudo-σ)$[13b/14b] \rightarrow b[17a]$	20 100	0.118
a(pseudo-σ)$[14a] \rightarrow b[17a]$	24 600	0
b(pseudo-σ)$[13a] \rightarrow b[17a]$	27 100	0.005
$b[17a] \rightarrow e[17b/18b]$ LF	18 800	
$b[17a] \rightarrow b[18a]$ LF	22 600	
$b[17a] \rightarrow a[19a]$ LF	25 000	
$e(\pi)[15b/16b] \rightarrow e[17b/18b]$	33 200	0.022
$a(\pi)[16a] \rightarrow e[17b/18b]$	33 700	0.282
$b(\pi)[15a] \rightarrow e[17b/18b]$	35 800	0.101

[a] The C_2 symmetry labels for each transition are shown in square brackets. [b] Oscillator strengths for LF transitions were not calculated.

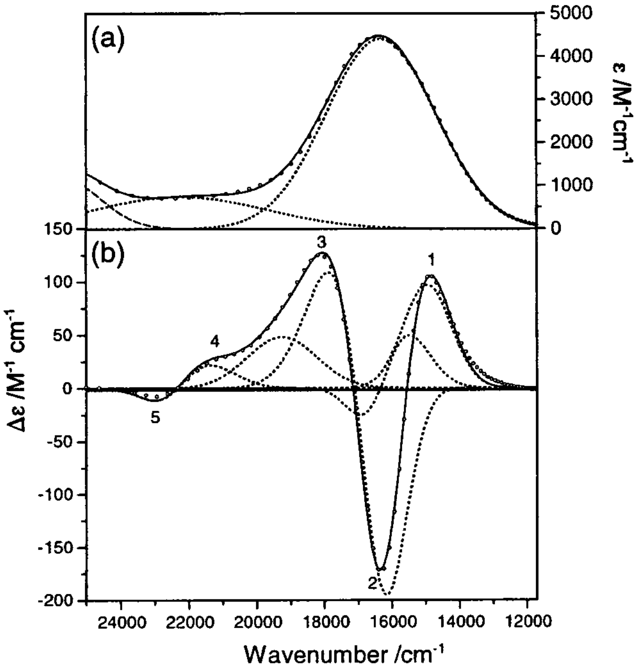

Figure 11. The simultaneous devolved fit of the 25 000−11 700 cm^{-1} region of the absorption (a) and MCD spectra (b) of $[PPh_4][MoO(SPh)_4]$. The higher energy regions of the spectra are shown in Figure 3. The component Gaussian functions are shown as dashed lines, and the total band shape as a solid line with one-third of the data points shown for clarity.

B. $[PPh_4][MoO(edt)_2]$. The low symmetry of $[MoO(edt)_2]^-$ results in all transitions except for $A_2 \leftarrow A_1$ being dipole allowed; however, it also removes all orbital degeneracy. Thus, all allowed optical transitions are polarized in one direction only and are formally MCD inactive. These transitions can gain MCD *C*-term intensity through spin−orbit coupling, which mixes in orthogonal transition moment character. The signs of the MCD transitions in C_{2v} can be predicted from a descent in symmetry in C_{4v}. Thus, $A_2 \leftarrow A_1$ and $B_1 \leftarrow A_1$ give rise to negative *C*-terms and $A_1 \leftarrow A_1$ and $B_2 \leftarrow A_1$ lead to positive *C*-terms. However, significant spin−orbit coupling into the ground state, as indicated by a deviation from the sum rule,[76] can lead to an apparent breakdown of these selection rules and MCD sign determination must then derive from explicit evaluations of the matrix elements in eq 1. Calculated transition energies and f_{calc} from the eight S *3p* SALCs to Mo $4d_{x^2-y^2}$ in $[MoO(edt)_2]^-$ are shown in Table 6. The values in Table 6 are derived from the spin unrestricted DFT calculations shown in Table 4 and Figure 10. The low symmetry of $[MoO(edt)_2]^-$ and the similar energies of the Sπ orbitals and the d orbital manifold make quantitative analysis of the spectra difficult. In particular, the energies of LMCT transitions to the $10a_1$ β orbital are underestimated, whereas the energies for LF transitions from $10a_1$ α to empty Mo d orbitals are overestimated. However, the DFT calculations clearly predict that the lowest energy LMCT transitions would be from three out-of-plane S π orbitals to the empty $10a_1$ β orbital, and these three LMCT transitions are calculated to occur at least 4000 cm^{-1} lower in energy than LMCT transitions from S pseudo-σ combinations to the $10a_1$ β orbital (Table 6). Furthermore, the LMCT transitions from the out-of-plane S π orbitals are predicted to be approximately 1 order of magnitude weaker than transitions involving their S pseudo-σ counterparts (Table 6). The proposed assignments for $[MoO(edt)_2]^-$ given below and in Table 2 draw heavily on the results for $[MoO(SPh)_4]^-$ described above and upon the qualitative molecular orbital scheme of Figure 9a.

The room-temperature CH_2Cl_2 solution absorption spectrum of $[PPh_4][MoO(edt)_2]$ from 11 100 to 25 000 cm^{-1} (Figure 4a) shows greater resolution of the LMCT bands than those of $[PPh_4][MoO(p\text{-}X\text{-}C_6H_4\text{-}S)_4]$ (X = H, Cl, OMe) (Figure 3a). The absorption spectrum from 11 100 to 25 000 cm^{-1} required a minimum of six Gaussians for adequate fitting (Figure 12a). Given the relative oscillator strengths for LMCT and LF transitions (see above), these bands may be assigned principally to LMCT. The MCD spectrum of $[PPh_4][MoO(edt)_2]$ within the

Table 6. Calculated Transition Energies and Oscillator Strengths for $[MoO(edt)_2]^-$ in C_{2v} Symmetry

transition	calculated energy/cm^{-1}	f_{calc}[a]
$6a_2(\pi)\beta \rightarrow 10a_1\,\beta$	2 500	0
$7b_1(\pi)\beta \rightarrow 10a_1\,\beta$	6 700	0.018
$8b_2(\pi)\beta \rightarrow 10a_1\,\beta$	8 300	0.022
$6b_1$(pseudo-σ) $\beta \rightarrow 10a_1\,\beta$	12 800	0.100
$9a_1(\pi)\beta \rightarrow 10a_1\,\beta$	14 200	0
$7b_2$(pseudo-σ) $\beta \rightarrow 10a_1\,\beta$	12 800	0.105
$5a_2$(pseudo-σ) $\beta \rightarrow 10a_1\,\beta$	19 900	0
$8a_1$(pseudo-σ) $\beta \rightarrow 10a_1\,\beta$	20 800	0.067
$10a_1\,\alpha \rightarrow 8b_1\,\alpha$ (LF)	27 900	
$10a_1\,\alpha \rightarrow 9b_2\,\alpha$ (LF)	29 200	
$10a_1\,\alpha \rightarrow 7a_2\,\alpha$ (LF)	34 100	
$10a_1\,\alpha \rightarrow 11a_1\,\alpha$ (LF)	38 000	
$6a_2(\pi)\alpha \rightarrow 8b_1\,\alpha$	23 200	0.360
$6a_2(\pi)\alpha \rightarrow 9b_2\,\alpha$	23 900	0.335
$7b_1(\pi)\alpha \rightarrow 8b_1\,\alpha$	27 300	0.010
$7b_1(\pi)\alpha \rightarrow 9b_2\,\alpha$	28 000	0

[a] Oscillator strengths for LF transitions were not calculated.

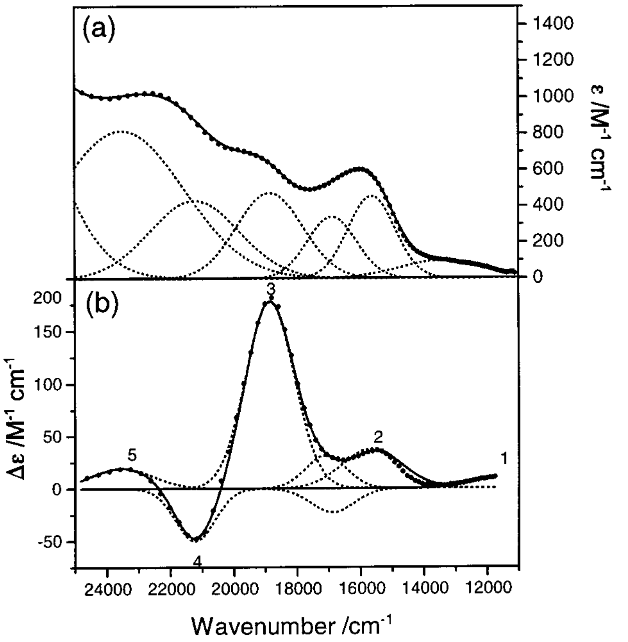

Figure 12. The simultaneous devolved fit of the 25 000−11 000 cm^{-1} region of the absorption (a) and MCD spectra (b) of $[PPh_4][MoO(edt)_2]$. The higher energy regions of the spectra are shown in Figure 4. The component Gaussian functions are shown as dashed lines, and the total band shape as a solid line with one-third of the data points shown for clarity.

14 000 to 25 000 cm^{-1} region was fitted simultaneously with four of the Gaussians centered on four of the visible absorptions and by two additional Gaussians (Figure 12b).

Band 1. The low intensity of band 1 in the absorption spectrum and the tailing of the more intense band at 15 900 cm^{-1}, band 2, made the estimate of its absorption maximum difficult by Gaussian deconvolution; however, its center can be obtained from the MCD spectrum in Figure 4c at 11 900 cm^{-1}. The positive sign of the band is consistent with a MCD forbidden $b_2(\pi) \rightarrow a_1(d_{x^2-y^2})$ transition that gains intensity through spin−orbit coupling. This transition occurs at a similar energy to the out-of-plane S $\pi \rightarrow d_{xy}$ transition in (L−N$_3$)MoO(toluene-3,4-dithiolate), and its weak intensity in absorption results from poor overlap of the out-of-plane $a_1(\pi)$ SALC with the in-plane $a_1(d_{x^2-y^2})$ orbital.[41] The oscillator strengths, f_{calc}, for the $b_2(\pi)$ and $b_1(\pi) \rightarrow a_1(d_{x^2-y^2})$ transitions in $[MoO(edt)_2]^-$ are comparable (0.022 and 0.018, respectively, Table 6) and both transitions may contribute to the weak feature at 12 800 cm^{-1} in the visible spectrum (Figure 4).

Band 2. This band is assigned to a b_2(pseudo-σ)$\rightarrow a_1(d_{x^2-y^2})$ transition. It corresponds to the first intense absorption in the visible spectrum of $[PPh_4][MoO(edt)_2]$ at 15 900 cm^{-1} (Figure 12a) and to positive intensity in the MCD spectrum (Figure 12b). A band of negative MCD intensity is required for a satisfactory fit for the MCD spectrum (Figure 12b) at 16 900 cm^{-1}, which is assigned to the corresponding b_1(pseudo-σ)$\rightarrow a_1(d_{x^2-y^2})$ transition (Table 2). The oscillator strengths, f_{calc}, for the b_2(pseudo-σ) and b_1(pseudo-σ)$\rightarrow a_1(d_{x^2-y^2})$ transitions in $[MoO(edt)_2]^-$ are comparable (0.105 and 0.100, respectively, Table 6) and both transitions contribute to the intense absorption at 15 900 cm^{-1} in the visible spectrum (Figure 4). In $[MoO(bdt)_2]^-$, the intense absorption band at ∼13 900 cm^{-1} with positive MCD intensity is assigned to transitions from the nonbonding S 3p(pseudo-σ) orbitals (Figure 9) to the Mo 4 d orbital in the *xy* plane ($10a_1$ β, Figure 10), which is consistent with our assignment for band 2.[64]

On the basis of assignments for the UV/vis and MCD spectra of $[MoOCl_4]^-$, (L−N$_3$)MoO(bdt), and $[PPh_4][MoO(SPh)_4]$ (see above), the first LF band is expected to appear in the 16 000 cm^{-1} region. Centering Gaussians at 15 600 and 16 900 cm^{-1} requires the overlap of a positive feature at 17 100 cm^{-1} to simultaneously reproduce the UV/vis absorption and MCD spectra within this range. This band is assigned to the LF $a_1(d_{x^2-y^2}) \rightarrow b_2(d_{yz})$ transition that occurs at an energy that is considerably less than that estimated by DFT calculations (27 900 cm^{-1}, Table 6). This overestimation may be due in part to the idealized C_{2v} symmetry (Figure 2f), which imposes an eclipsed conformation for the C−C backbone of edt^{2-}. In the crystal structure of $[PPh_4][MoO(edt)_2]$,[56] the two MoS_2 planes are slightly twisted with respect to one another (see below), and one edt^{2-} chelate adopts a staggered conformation. These distortions may somewhat attenuate the ligand field from that predicted by the DFT calculations.

Band 3. Band 3 is assigned to a a_1(pseudo-σ)$\rightarrow a_1(d_{x^2-y^2})$ transition, which appears at 18 900 cm^{-1} in the visible spectrum (Figure 12a). DFT calculations place this transition at 20 800 cm^{-1} (Table 6), pointing to a significant interaction between the S a_1(pseudo-σ) and Mo $a_1(d_{x^2-y^2})$ orbitals that may provide a mechanism for modulating the energy of the redox active orbital (see below). In (L−N$_3$)MoO*S*$_2$ complexes, the analogous pseudo-σ bonding to antibonding transition occurs in the 19 100−20 000 cm^{-1} range, and excitation within this band shows resonance Raman enhancement of the Mo−S modes.[54] In $[PPh_4][MoO(bdt)_2]$, the absorption at ∼19 200 cm^{-1} that is strongly positive in the MCD spectrum is assigned to this in-plane transition.[62,64]

Bands 4 and 5. The a_2(pseudo-σ)$\rightarrow a_1(d_{x^2-y^2})$ transition is expected to occur in this region on the basis of a comparison with the assignments for $[PPh_4][MoO(SPh)_4]$. In C_{2v} symmetry, this transition is orbitally forbidden, which is inconsistent with the high intensity observed for the band in the visible spectrum. Consequently, bands 4 and 5 are assigned to a $b_{1,2}(\pi) \rightarrow b_{1,2}(d_{xz,yz})$ LMCT transitions of opposite sign.

Bands 6 and 7. Bands 6 and 7 (Figure 4) share the same profile as bands 10 and 11 in the MCD spectrum of $[PPh_4][MoO(SPh)_4]$ and are easily assigned as $a_2(\pi) \rightarrow b_{1,2}(d_{xz,yz})$ LMCT. They occur at a lower energy than in $[PPh_4][MoO(SPh)_4]$, consistent with the S *3p* π orbitals being raised in energy relative to those in $[PPh_4][MoO(SPh)_4]$. The destabilization of the S 3p π orbitals in $[PPh_4][MoO(edt)_2]$ is overestimated by the DFT calculations (Table 6), but the separation between the calculated energies for the $6a_2(\pi)\alpha,\beta \rightarrow 8b_1(d_{xz})\alpha,\beta$ and $9b_2(d_{yz})\alpha,\beta$ transitions (approximately 700 cm^{-1}) is reasonable for the negative and positive components of a negative pseudo-*A* term and is consistent with the observed MCD spectrum of [PPh$_4$][MoO(edt)$_2$].

In summary, assignments have been made for the MCD and absorption spectra of [PPh$_4$][MoO(edt)$_2$] (Table 2). We suspect that the $a_1(d_{x^2-y^2}) \rightarrow a_2(d_{xy})$ and the $a_1(d_{x^2-y^2}) \rightarrow b_1(d_{xz})$ LF transitions (occurring between 22 000 and 23 000 cm^{-1} and around 16 900 cm^{-1}, respectively) are masked by LMCT transitions in both the absorption and MCD spectra. The $a_{1,2}(\pi) \rightarrow a_1(d_{x^2-y^2})$ transitions were not observed in the visible/NIR and MCD spectra of [PPh$_4$][MoO(edt)$_2$] due to their weak oscillator strength (Table 6) and the lack of appreciable metal character in the $a_{1,2}(\pi)$ orbitals (Table 4) that would provide gains in MCD intensity through spin−orbit coupling. Our assignments show a clear separation in intensity and energy for transitions arising from S 3p π and S 3p pseudo-σ orbitals to the Mo $a_1(d_{x^2-y^2})$ orbital in [PPh$_4$][MoO(edt)$_2$] (Table 2), with the transitions from S 3p π orbitals being at lower energy and less intense.

IV. Discussion

Our interpretation of the MCD and absorption spectra of [PPh$_4$][MoO(*p*-SC$_6$H$_4$X)$_4$] (X = H, Cl, OMe) and [PPh$_4$][MoO(edt)$_2$], supported by DFT calculations, points to a major role for the geometry of the ligand backbone and a smaller effect for the electron-donating and -withdrawing substituents in controlling the energies of the S 3p lone pair and Mo 4d orbitals. This is supported by the identity of the *g* values for X = H, Cl, OMe and by the similar profiles of the MCD spectra of [PPh$_4$][MoO(*p*-SC$_6$H$_4$X)$_4$] (Figure 3b,c). Ab initio calculations on the free [*p*-SC$_6$H$_4$X]$^-$ ligands point toward a comparable separation in energy between the b_1 and b_2 S lone pairs (0.81, 0.82, and 0.90 eV for X = H, Cl and OMe, respectively) and a relative lowering and raising of the entire ligand orbital manifold that is dependent on the nature of the para substituent (−2.248, −2.842, and −2.414 eV for X = H, Cl, and OMe, respectively). Thus, the electronic spectra and the *g* values are primarily determined by the donor atoms and coordination geometry of the oxo-Mo(V) center. However, the relative energies of different [MoO(*p*-SC$_6$H$_4$X)$_4$]$^-$ complexes do depend on the nature of X, the remote substituent, as illustrated by the strong correlation of their Mo(V/IV) electrochemical potentials with the Hammett parameter, σ.[66] Similar effects have also been observed in *cis,trans*-(L-N_2S_2)Mo^{V}O(SR) [L-$N_2S_2H_2$ = *N,N*-dimethyl-*N,N*-bis(mercaptophenyl)ethylenediamine, R = *p*-C$_6$H$_4$-Y (Y = CF$_3$, Cl, Br, F, H, CH$_3$, CH$_2$CH$_3$ and OCH$_3$)] where the nature of the para substituent leads to small variations in *g* values but large differences in the Mo(V/IV) reduction potential.[81]

Our results for [PPh$_4$][MoO(edt)$_2$] show that the S π SALCs are at least 3000−4000 cm^{-1} higher in energy than the S pseudo-σ orbitals (Table 2), and there is a general shift to lower energy for LMCT transitions from the S π SALCs in [PPh$_4$][MoO(edt)$_2$] relative to the corresponding transitions in [PPh$_4$][MoO(*p*-SC$_6$H$_4$X)$_4$]. This is most apparent for the $a_{1,2}(\pi) \rightarrow b_{1,2}(d_{xz,yz})$ transitions that occur at 27 600 and 29 900 cm^{-1} in [PPh$_4$][MoO(edt)$_2$] compared to the corresponding a,b$\rightarrow$e($d_{xz,yz}$) transitions at 31 500 cm^{-1} in [PPh$_4$][MoO(SPh)$_4$]. The decrease in energy of the S π LMCT results from an increase in repulsion between the S π orbitals (Figure 6a), a consequence of the rigid geometry imposed on the S atoms by the C−C backbone of edt^{2-}.

In the visible absorption spectrum of [PPh$_4$][MoO(edt)$_2$] (Figure 4b), transitions from the a_1, b_1 and b_2 pseudo-σ orbitals to the Mo $4d_{x^2-y^2}$ orbital are well-resolved. Their identical oscillator strengths (Table 2), which are at least three times greater than those for the S π transitions to Mo $4d_{x^2-y^2}$, suggest that there is considerable covalency between the Mo center and the S ligands derived from interactions involving the S pseudo-σ combinations in the ground state. The specific interactions between the a_1, b_1 and b_2 pseudo-σ SALCs and the Mo $4d_{x^2-y^2}$, $4d_{xz}$, and $4d_{yz}$ orbitals are detailed in Figure 13. Evidence for the overlap of the a_1 pseudo-σ orbital and Mo $4d_{x^2-y^2}$ also derives from spectroscopic studies on (L−N$_3$)MoO(bdt), which lead to the proposal of a σ pathway for the electronic coupling of the Mo center to the pyranopterin at the active sites of oxomolybdoenzymes.[54] Our studies reveal a second interaction between the b_1 and b_2 pseudo-σ orbitals and $b_1(d_{xz})$ and $b_2(d_{yz})$ that permits direct communication between the Mo≡O bond with the σ framework of the ene-1,2-dithiolate ligand. Unrestricted DFT calculations on [MoO(edt)$_2$]$^-$ indicate that these interactions may compete effectively with electron donation from the oxo group ($9b_2$, Mo $4d_{yz}$ = 51.4%, total S p = 21.9% and total O p = 20.6%, Table 4). S participation in the Mo≡O bond is also apparent in [MoO(SMe)$_4$]$^-$, where the total S p percent character in the e(17b, 18b) orbitals (14.1%) is comparable to that of the total oxo contribution (19.9%) (Table 3).

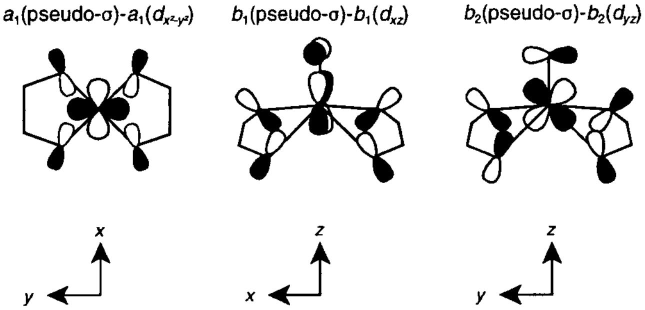

Figure 13. The S 3p(pseudo-σ) interactions with the Mo $4d_{x^2-y^2}$, $4d_{yz}$, and $4d_{xz}$ orbitals in [MoO(edt)$_2$]$^-$.

In addition, the energies of the LF bands in [PPh$_4$][MoO(SPh)$_4$] (17 000 cm^{-1}, Figure 9b) and [PPh$_4$][MoO(edt)$_2$] (15 900 and 18 700 cm^{-1}, Figure 10b) are higher than the corresponding transitions in [MoOCl$_4$]$^-$ (16 000 cm^{-1})[41] and (L−N$_3$)MoO(bdt) (15 800 cm^{-1}).[54] If the first LF transition were completely dominated by the Mo≡O group, then the greater experimental ligand field splittings would be indicative of stronger Mo≡O bonds in MoOS_4 complexes. However, the Mo≡O stretching frequencies for [MoO(SR)$_4$]$^-$ compounds (R = C$_6$H$_5$, 4-CH$_3$C$_6$H$_4$, 4-ClC$_6$H$_4$, 4-FC$_6$H$_4$, and 2,6-Cl$_2$C$_6$H$_3$, υ = 927−982 cm^{-1}).[66] and [MoO(edt)$_2$]$^-$ (υ = 917 cm^{-1})[82] occur at lower energy than those of other five-coordinate oxomolybdenum complexes, e.g. [MoOX$_4$]$^-$ (X = Cl, Br, I, υ = 1000−1020 cm^{-1}).[66,83] Thus, the larger ligand field splittings of MoOS_4 centers are accompanied by *weaker* Mo≡O bonds. Tables 3 and 4 show that the S pseudo-σ $6b_1$ and $7b_2$ orbitals in [MoO(edt)$_2$]$^-$ and the S e(π) orbitals in [MoO(SMe)$_4$]$^-$ contain substantial antibonding contributions from the O π orbitals. The total contributions of Mo $4d_{xz,yz}$ and S $3p_{x,y,z}$ in these orbitals are similar in the two compounds, but the $6b_1$ and $7b_2$ orbitals in [MoO(edt)$_2$]$^-$ show substantially greater antibonding contributions from the O π orbitals than do the corresponding e(π)

---

(81) Mader, M. L.; Carducci, M. D.; Enemark, J. H. *Inorg. Chem.* **2000**, *39*, 525−531.

(82) Donahue, J. P.; Goldsmith, C. R.; Nadiminti, U.; Holm, R. H. *J. Am. Chem. Soc.* **1998**, *120*, 12869−12881.

(83) Garner, C.; Hill, L.; Howlander, N.; Hyde, M.; Mabbs, F.; Routlege, V. *Less-Common Met.* **1977**, *54*, 27.

orbitals in $[MoO(SMe)_4]^-$, consistent with $[MoO(edt)_2]^-$ having the lowest Mo≡O stretching frequency of known $MoOS_4$ complexes.[66,82] Thus, for $MoOS_4$ centers the electron donation by the S ligands may be sufficient to limit the dominance of the Mo≡O bonding within the ligand field manifold. This conclusion is also supported by PES studies on $(L-N_3)MoES_2$ (E = O, S, NO) that suggest an "electronic buffer" role for the ene-1,2-dithiolate ligand that competes with E in its bonding to the Mo.[53]

The relative energies of the S 3p orbitals together with the relative differences in covalency of the ground states in $[PPh_4][MoO(p\text{-}SC_6H_4X)_4]$ and $[PPh_4][MoO(edt)_2]$ are manifest in their *g* values (Figures 3c and 4d). These anomalously high g_1 and g_{zz} values have been attributed to contributions from a combination of spin−orbit coupling, metal ligand covalency, and a mixing of low-energy charge transfer states, eq 4:[52]

$$g_{zz} = 2.0023 - \sum_n \left(\frac{\xi_{Mo}(\langle 0|L_z|n\rangle\langle n|L_z|0\rangle)}{\Delta E_{d-d}} \right) + \sum_n \left(\frac{\xi_S(\langle 0|L_z|n\rangle\langle n|L_z|0\rangle)}{\Delta E_{LMCT}} \right) \quad (4)$$

where ξ is the spin−orbit coupling coefficient, ΔE is the transition energy between ground state (0) and excited state (*n*) and L_z is the angular momentum operator. In C_4 symmetry the mixing between the ^2B ground state and excited states of ^2B symmetry leads to an increase in $g_{\|}$. In C_{2v} symmetry, increases in g_{zz} result from the mixing of $^2A_2$ excited states into the $^2A_1$ ground state. In both complexes LMCT involving these symmetries originates from pseudo-σ S 3p orbitals that possess a highly covalent interactions with the Mo $4d_{x^2-y^2}$ and Mo $4d_{xy}$ orbitals in $[PPh_4][MoO(p\text{-}SC_6H_4X)_4]$ and with the Mo $4d_{xy}$ orbital in $[PPh_4][MoO(edt)_2]$. The near identity of the electronic and MCD spectra for the $[PPh_4][MoO(p\text{-}SC_6H_4X)_4]$ compounds below about 22 000 cm^{-1} (Figure 3) completely accounts for their identical EPR spectra following eq 4.

The ^{95}Mo hyperfine coupling constants, A_{zz}, for $[PPh_4][MoO(SPh)_4]$ and $[PPh_4][MoO(edt)_2]$ are 52.3 and 49.4 × 10^4 cm^{-1}, respectively (Figures 3 and 4), and are determined principally by the composition of the ground-state orbital. An expression for A_{zz} for a complex possessing a d_{xy} or $d_{x^2-y^2}$ ground state is given in eq 5:[79]

$$A_{zz} = A_{iso} + P\left(\frac{2}{3}\Delta g_{zz} - \frac{(\Delta g_{xx} + \Delta g_{yy})}{3} - \frac{4}{7}\alpha^2 + \frac{3(\Delta g_{xx} + \Delta g_{yy})}{14} \right) \quad (5)$$

$$A_{iso} = P\left(-\alpha^2\kappa + \frac{(\Delta g_{zz} + \Delta g_{xx} + \Delta g_{yy})}{3} \right)$$

where *P* is the electron−nuclear dipolar coupling parameter ($P = -67.6 \times 10^4$ cm^{-1} for Mo(V)),[79] κ = Fermi contact parameter that expresses the contribution of s electron density, α = molecular orbital coefficient for the half-occupied metal orbital, and $\Delta g_{ii} = g_{ii} - 2.0023$ for $i = x, y, z$, where g_{ii} is the *g*-factor. For $[PPh_4][MoO(SPh)_4]$ and $[PPh_4][MoO(edt)_2]$ eq 5 reduces to

$$A_{zz} = P\left(-\alpha^2\left(\kappa + \frac{4}{7} \right) + G \right) \quad (6)$$

$$G = \Delta g_{zz} + \frac{3(\Delta g_{xx} + \Delta g_{yy})}{14}$$

where G = 0.034 and 0.041, respectively, representing a difference in A_{zz} of 0.5 × 10^{-4} cm^{-1} between the two complexes. Thus, the difference in A_{zz} for $[PPh_4][MoO(SPh)_4]$ relative to $[PPh_4][MoO(edt)_2]$ of ∼3 × 10^{-4} cm^{-1} (Figures 3 and 4) must be determined principally by differences in α and κ for the two compounds. DFT calculations (Tables 3 and 4) reveal that α^2 is 0.53 and 0.71 for $[MoO(SMe)_4]^-$ and $[MoO(edt)_2]^-$, respectively, which would lead to a larger A_{zz} for the latter complex, in contrast to experiment. Consequently, the lower value of A_{zz} for $[PPh_4][MoO(edt)_2]$ must result from a value of κ that is lower for $[MoO(edt)_2]^-$. For unpaired electrons in d orbitals, Fermi contact arises from spin polarization of core s electrons. However, an additional contribution to the Fermi contact parameter can arise through configuration interaction that, in C_{2v} symmetry, allows the direct admixture of the 5s orbital into the half-occupied $4d_{x^2-y^2}$. This additional contribution, which would be of opposite sign to the spin polarization contribution, is forbidden for $[MoO(SPh)_4]^-$ in C_4 symmetry, and consequently $A_{zz}([MoO(SPh)_4]^-) > A_{zz}([MoO(edt)_2]^-)$.

In our previous studies of $LMoOS_2$ compounds with chelated 1,2-dithiolate ligands we showed that the number of MCD bands and their position in the spectrum is primarily determined by the orientation of the S p orbitals on the thiolate ligands and is relatively insensitive to electron delocalization in the chelate skeleton.[41,54] The $[MoO(edt)_2]^-$ anion investigated here has a saturated C_2H_4 ligand skeleton, whereas the $[MoO(bdt)_2]^-$ anion investigated previously[61,64] has an unsaturated ene-1,2-dithiolate chelate skeleton. Comparison of the metrical details for the $[Mo^VOS_4]^-$ centers of $[PPh_4][MoO(edt)_2]$[56] and $[PPh_4][MoO(bdt)_2]$[59] shows that their Mo═O and Mo−S distances and their S−Mo−S angles are nearly identical. The distance of the Mo atom from the mean S_4 plane (0.76[56] and 0.74 Å[59]) and the fold angle (θ_{fold}, Figure 14) between the two MoS_2 planes are very similar (θ_{fold} = 142.4° [56] and 143.9° [59]). The twist angle (θ_{twist}, Figure 14) between the MoS_2 planes differs slightly for the two compounds (θ_{twist} = 8.7° for $[PPh_4][MoO(edt)_2]$[56] and 2.2° for $[PPh_4][MoO(bdt)_2]$[59]). On the basis of the close structural similarity of their $[MoOS_4]^-$ cores, the absorption and MCD spectra of $[PPh_4][MoO(edt)_2]$ (Figure 4b,c) and $[PPh_4][MoO(bdt)_2]$[61,64] are also expected to be similar to one another.[41]

The MCD spectra of $[PPh_4][MoO(edt)_2]$ (Figure 4b,c) and $[PPh_4][MoO(bdt)_2]$[61] are strikingly similar above ∼17 000 cm^{-1}. At lower energies $[PPh_4][MoO(edt)_2]$ (Figure 4b,c) shows weak positive features at 11 900 and 15 400 cm^{-1}, whereas $[PPh_4][MoO(bdt)_2]$[61,64] exhibits a single strong broad positive feature at ∼13 500 cm^{-1} that is assigned[64] to charge-transfer transitions from nonbonding S 3p(pseudo-σ) orbitals (Figure 9) to the Mo 4 d orbital in the *xy* plane ($10a_1\ \beta$, Figure 10). In our analysis of the absorption and MCD spectra of $[PPh_4][MoO(edt)_2]$, we assign the transition at 15 400 cm^{-1} to $b_2(\text{pseudo-}\sigma) \rightarrow a_1(d_{x^2-y^2})$ LMCT with $b_1(\text{pseudo-}\sigma) \rightarrow a_1(d_{x^2-y^2})$ LMCT and $a_1(d_{x^2-y^2}) \rightarrow b_2(d_{yz})$ LF components and that at 18 800 cm^{-1} to $a_1(\text{pseudo-}\sigma) \rightarrow a_1(d_{x^2-y^2})$ LMCT, respectively. These assignments parallel those made for the features at ∼13 500 and ∼20 000 cm^{-1} in the absorption and MCD spectra of $[PPh_4][MoO(bdt)_2]$.[64] The higher energy of the $a_1(\text{pseudo-}\sigma) \rightarrow a_1(d_{x^2-y^2})$ LMCT transition in $[PPh_4][MoO(bdt)_2]$ suggests a greater covalent interaction between the a_1 pseudo-σ SALC and the Mo $4d_{x^2-y^2}$ orbital (Figure 13) in this complex relative to $[PPh_4][MoO(edt)_2]$. Presumably this results from the conjugated chelate skeleton of the bdt ligand that provides more efficient coupling between the sulfur atoms

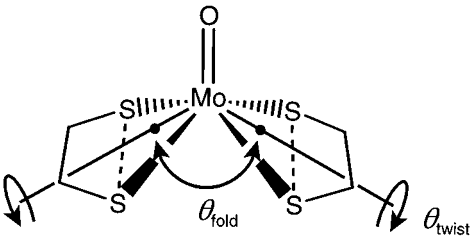

Figure 14. Illustration of the angles used to describe the relative orientations of the two MoS_2 planes: θ_{fold} is the angle formed between the Mo atom and the midpoints of the two S···S vectors; θ_{twist} describes the twist of the two MoS_2 planes relative to one another. For square pyramids and trigonal prisms, $\theta_{twist} = 0°$.

and the Mo center. This is also supported by the generally larger values of ϵ and $\Delta\epsilon$ for the $[PPh_4][MoO(bdt)_2]$ absorption and MCD spectra.[61,64] In summary, the analysis of the electronic structures of $[Mo^VOS_4]^-$ centers developed here provides self-consistent descriptions for the MCD and absorption spectra of the $[MoO(SR)_4]^-$, $[MoO(edt)_2]^-$, and $[MoO(bdt)_2]^-$ complexes.

V. Implications for DMSO reductase

The current X-ray crystallographic data for the DMSO reductases show that, despite the high degree of sequence homology, there are significant structural differences in the description of the coordination sphere of the Mo center at the active sites for enzymes isolated from different sources. These include the proposals of mono-oxo Mo(VI)[25] and di-oxo Mo(VI)[7,10] centers for the oxidized forms of the enzymes from *Rs* and *Rc*, respectively, and differences in the nature of the ene-1,2-dithiolate coordination. Some of these discrepancies have been resolved by complimentary EXAFS studies[18] on DMSO reductase from *Rs* that corroborate a mono-oxo Mo(VI)−*des*-oxo Mo(IV) cycle that was proposed from a recent resonance Raman study.[26] This mechanism is similar to that originally presented in the light of the X-ray crystallographic results on DMSO reductase from *Rs*[25] but differs in that the number of S donors presented to the Mo atom by the ene-1,2-dithiolate ligands remains invariant at all points in the cycle. A very recent high-resolution X-ray structure of *Rs* DMSO reductase shows that the Mo site is discretely disordered.[84] One of the components has all four S atoms of the two ene-1,2-dithiolate groups coordinated to the Mo atom, as proposed from the resonance Raman study.[26] While there are no X-ray crystallographic results for the Mo(V) form of the DMSO reductases, the mechanism proposed from the resonance Raman results infers a [Mo(ene-1,2-dithiolate)$_2$] center with the coordination sphere about the Mo(V) completed by O−Ser and hydroxyl ligands. Resonance Raman results also indicate that these ligands may become displaced by glycerol in the inhibited Mo(V) form from *Rs*.[26]

The room-temperature absorption spectrum of the glycerol-inhibited form of DMSO reductase[34] consists of broad bands centered at 14 700, 17 600, and 26 400 cm^{-1}. The spectrum is similar to that of $[PPh_4][MoO(edt)_2]$ (Figure 4b), and by comparison the absorption bands can be assigned reasonably to low-energy LMCT. However, the MCD spectrum for the glycerol-inhibited form of DMSO reductase was obtained before it was known that the enzyme can exhibit multiple Mo(V) EPR signals[19] and before the multiple crystal structures of DMSO reductases[6,7,10,25,84] raised the possibility that under certain conditions only one of the ene-1,2-dithiolate ligands is actually coordinated to the Mo atom.[6] Thus, the actual structure of the Mo(V) center giving rise to the glycerol-inhibited MCD signal is not known, and it is possible that the observed MCD spectrum results from a composite of more than one Mo(V) species.[84] Deeper insight into the electronic structure of the active site of DMSO reductase must await additional spectroscopic studies on well-characterized enzyme samples as well as studies on structurally characterized complexes with *des*-oxo-Mo centers.[82]

The original interpretation of the MCD spectrum of the glycerol-inhibited form of DMSO reductase was based upon π-ene-1,2-dithiolate→Mo(V) CT in a fragment of C_{2v} symmetry.[34] Our results show that LMCT from S pseudo-σ combinations to the Mo 4d orbitals must be included in addition to LMCT from the S π SALCs. The most recent high-resolution X-ray crystallographic study of *Rs* DMSO reductase reveals that the six-coordinate component of the disordered active site exhibits distorted trigonal prismatic coordination about the Mo atom with four S atoms, an oxo group, and an O−Ser ligand.[84] The relative orientation of the MoS_2 planes of the two ene-1,2-dithiolate ligands gives $\theta_{twist} = 27°$ and $\theta_{fold} = 129°$ (Figure 14). If the geometry of the ene-1,2-dithiolate ligands is largely retained in the Mo(V) forms of the enzymes, then the differences between the MCD spectra of $[PPh_4][MoO(SPh)_4]$ ($\theta_{twist} = 1.6°$ and $\theta_{fold} = 140.3°$) and $[PPh_4][MoO(edt)_2]$ ($\theta_{twist} = 8.7°$ and $\theta_{fold} = 142.4°$), and the glycerol-inhibited Mo(V) forms of DMSO reductase[34] may also arise from differences in θ_{twist} and θ_{fold} about the Mo atom in these centers.

Nevertheless, our analysis of the MCD and absorption spectra of $[PPh_4][MoO(p\text{-}SC_6H_4X)_4]$ and $[PPh_4][MoO(edt)_2]$ points to a significant role for the ligand backbone in determining the spectroscopic properties of the Mo center by controlling the geometry of the S lone pairs presented to the Mo atom. This is supported by the differences between the absorption, MCD, and EPR spectra of $[PPh_4][MoO(p\text{-}SC_6H_4X)_4]$ and $[PPh_4][MoO(edt)_2]$ and by the DFT calculations on $[MoO(SMe)_4]^-$ that reveal strong variations in the energies of the S 3p lone pair and Mo 4d orbitals with O−Mo−S−C(α) dihedral angle (Figure 6a). We highlight, in our analysis of the MCD and absorption spectra of $[PPh_4][MoO(edt)_2]$, three pseudo-σ interactions that can control the relative energies of the Mo $4d_{x^2-y^2}$ and $4d_{xz,yz}$ orbitals. The pseudo-σ−$d_{x^2-y^2}$ interaction provides a mechanism for modulating the reduction potential of the active site by the ene-1,2-dithiolate of the pyranopterin and provides a σ-pathway for electron transfer to this redox active orbital during active site regeneration.[54] The pseudo-σ−d_{xz} and pseudo-σ−d_{yz} interactions (Figure 13) weaken the Mo≡O bond and prime the oxo group for protonation during the regenerative phase of the catalytic cycle. This effect should be enhanced in the active site of DMSO reductase by the small fold angle ($\theta_{fold} = 129°$). The overlap of the S pseudo-σ orbitals of the planar ene-1,2-dithiolate framework with the Mo 4d orbitals will also be dependent on θ_{twist}. Thus, the distorted geometry at the active sites of the DMSO reductases may represent a Mo center which is poised at an optimum reduction potential for DMSO reduction and in which the electronic structure is tuned to promote Mo≡O cleavage during the reduction of the active site from the mono oxo-Mo(VI) to the *des*-oxo-Mo(IV) form. In addition, X-ray crystallography reveals a Mo(ene-1,2-dithiolate)$_2$ geometry that is largely retained in the oxidized and reduced forms of DMSO reductase from *Rc*,[7,10] suggesting that at this geometry the ligand field is dominated by pseudo-σ and π donation by the ene-1,2-dithiolate ligands. This allows facile oxygen atom transfer with the minimum change in reorganization energy at the active site.

---

(84) Li, H.-K.; Temple, C.; Rajagopalan, K. V.; Schindelin, H. *J. Am. Chem. Soc.* **2000**, *122*, 7673−7680.

Acknowledgment. We thank The Royal Society (J.M.), NIH (GM-37773, J.H.E), USDA (94-37305-0576, J.H.E.), and NSF (CHE 9980549, E.I.S.) for financial support. We thank Dr. H. Schindelin for a preprint of ref 84. We thank Dr. M. L. Kirk for preprints of refs 63 and 64 and helpful discussions. We thank H. Joshi for assistance with the analysis of the coordination geometries.

Supporting Information Available: Table S1, coordinates used in the DFT calculations for $[MoO(SMe)_4]^-$ in C_4 symmetry with a O−Mo−S−C(α) dihedral angle = 58.8°; Table S2, coordinates used in the DFT calculations for $[MoO(edt)_2]^-$ in C_{2v} symmetry; and Table S3, results of unrestricted DFT calculations for the frontier orbitals of $[MoO(edt)_2]^-$. This material is available free of charge via the Internet at http://pubs.acs.org.

IC0005846